CERN-THESIS-2010-310

KATHOLIEKE UNIVERSITEIT
LEUVEN

FACULTEIT WETENSCHAPPEN
Departement *Natuurkunde & Sterrenkunde*
Afdeling *Kern- en Stralingsfysica*

Decay Study of ^{200}Fr and ^{182}Tl

door

Marijke KEUPERS

Promotor: Prof. Dr. Mark Huyse
Begeleider: Dr. Martin Venhart

Proefschrift ingediend tot het behalen van de graad van Master in de Natuurkunde

Academiejaar 2009-2010

Dankwoord

Gedurende vijf jaar heb ik mogen genieten van een degelijke opleiding aan de K.U.Leuven. De vijf jaar zijn bijna voorbij voor mij en deze thesis zou het summum moeten zijn van mijn masteropleiding in de kernfysica.
Ik heb het hele traject niet op mijn eentje afgelegd. Tijdens deze vijf jaar, en in het bijzonder tijdens mijn thesis, ben ik door een hele hoop mensen geleid, geholpen en gesteund. Ik bedank graag even de volgende personen, voor alle tijd en moeite die ze in mij hebben gestoken.

In de eerste plaats dank ik prof. Mark Huyse en prof. Piet Van Duppen, voor de mogelijkheid die zij hebben aangeboden om mijn thesis in de spectroscopie-groep van het IKS te doen. Zowel tijdens de lessen als daarbuiten stonden zij altijd klaar met raad en daad. Een extra dank gaat naar mijn promotor, prof. Mark Huyse, voor de hulp bij de structuur van de thesis en voor het nalezen ervan.

Next, a really big thank you goes to Martin, who helped me throughout the whole year. Even when he didn't have a lot of time, he was always ready to help me with all my problems concerning physics, computer programs, English,... . His experience contributed to my thesis, as well as his competence to create an enjoyable environment. I should also thank prof. Andrei Andreyev, for the interesting discussions, Thomas for his help with the analysis of the Fr data and Dieter for the assistance with the root programs. Martin, Jytte and Thomas, thank you for your company and fun moments in our office and off course also for all the help.

Dankjewel aan alle leden van het IKS. Ik denk dat er weinig groepen zijn waar, terwijl er hard wordt gewerkt, zo'n geweldige sfeer heerst en waar masterstudenten zo goed opgevangen worden. Ik heb op het IKS een zeer aangename en interessante tijd beleefd.
Nele, Wim en Bart wil ik bedanken om zo'n leuke medestudenten te zijn. Vooral Nele, ik vond het tof om zo vaak jouw partner te zijn bij allerlei groepswerken.

Ik wil ook mijn medestudenten, die geen kernfysica zijn gaan studeren, bedanken. Daniel, Jeroen, Bram en Lucie, bedankt voor de toffe vijf jaar. Michiel en Steven, bedankt voor de ontspannende momenten, zeker wanneer ik ze echt nodig had. Bedankt Ingrid en Katleen, het is leuk om twee zo'n geweldige zussen te hebben.
Jan, bedankt voor de oneindige steun en geduld die je mij hebt gegeven deze vijf jaar. Bedankt om mij aan het lachen te krijgen wanneer ik gestresseerd en moe ben. Bedankt om steeds klaar te staan.

Tenslotte bedank ik mijn mama en mijn papa. Voor het vertrouwen dat zij in mij hebben gesteld, voor alle mogelijkheden die ze aan mij hebben gegeven, voor alle steun die ik heb gekregen, niet alleen deze vijf jaar, maar al 23 jaar lang.

Samenvatting

Wanneer een kern β-verval ondergaat en de energie van de geëxciteerde dochterkern vergelijkbaar is met of groter is dan de hoogte van de fissiebarrière, dan kan de dochterkern bijna onmiddellijk splitsen in twee kleinere fragmenten. Dit type verval noemt men β-vertraagde fissie. β-vertraagde fissie is waargenomen in verschillende kernen in de neutronarme Pb-regio. β-vertraagde fissie concurreert met elektromagnetische vervalswijzen van de dochterkern.

Het eerste deel van deze thesis concentreert zich op het bestuderen van het α-verval van ^{200}Fr. β-vertraagde fissie werd recent ontdekt in ^{196}At. Het α-verval van ^{200}Fr werd bestudeerd om een betere waarde te vinden voor de β-branching verhouding van de dochterkern ^{196}At. Deze waarde is belangrijk om de β-vertraagde fissie nauwkeurig te onderzoeken.
Het tweede deel van de thesis heeft betrekking op de studie van de γ-stralen die volgen op het β-verval van ^{182}Tl. De γ-stralen werden bestudeerd om de kernstructuur van ^{182}Tl en ^{182}Hg te onderzoeken. Dit zijn twee belangrijke isotopen waarin vorm-coëxcistentie voorkomt.

Beide experimenten werden uitgevoerd in ISOLDE in CERN. De radio-actieve bundel die werd geproduceerd door ISOLDE werd geïmplanteerd op een zeer dunne koolstoffolie. Op een wiel in de "windmill chamber" zijn tien zulke dunne koolstoffolies aangebracht. Het wiel werd elke supercyclus gedraaid, zodat de bundel op een nieuwe folie geïmplanteerd kon worden. De folie waar de bundel eerst op geïmplanteerd werd, wordt op deze manier van het implantatiestation naar het vervalstation gebracht. Vier Si-detectoren werden gebruikt om de α-deeltjes en de fissiefragmenten te meten: twee langs de voor- en achterkant van de folie in het implantatiestation, twee langs de voor- en achterkant van de folie in het vervalstation. Een Miniball clusterdetector met drie Ge-kristallen, achter het implantatiestation, werd gebruikt om de γ-stralen te detecteren.

Tijdens het eerste experiment, waarbij ^{200}Fr geïmplanteerd werd, ontsnapte een significant deel van de dochterkernen ^{196}At uit de koolstoffolie door de terugslag van het uitgestuurde α deeltje. De data werd gecorrigeerd voor dit effect en een betere waarde voor de EC/β^+-branching verhouding van ^{196}At werd verkregen en vergeleken met de vroegere gepubliceerde waarde.

De halfwaardetijd van ^{182}Tl werd bepaald door de γ-stralen, die volgen op het β-verval van de kern, te bestuderen. Vervolgens zijn de $\gamma\gamma$-coïncidenties onderzocht om dan uiteindelijk het niveauschema van ^{182}Hg op te stellen. Er is een transitie met een $E0$ component waargenomen tussen twee toestanden met een andere vervorming.

Summary

Recently, the β-delayed fission was observed in different nuclei in the neutron-deficient Pb region. β-delayed fission is a rare process when a nucleus undergoes β decay and the excited energy of the daughter nucleus is high enough, the daughter nucleus can almost immediately fission into two smaller fragments with a certain probability. This process competes with electromagnetic decay of the daughter nucleus. The study of β-delayed fission requires information on the parent and daughter nucleus.

The first part of the thesis deals with the α-decay study of ^{200}Fr. βDF was recently discovered in ^{196}At. The α-decay study of ^{200}Fr was dedicated to find a improved value for the β-branching ratio of its daughter nucleus ^{196}At, which is needed for understanding the β-delayed fission.
The second part of the thesis, involved the study of γ rays subsequent to the β decay of ^{182}Tl. The γ rays coming from the EC/β^+ decay were studied in order to gain information on the nuclear structure of ^{182}Tl and ^{182}Hg, which are important isotopes to study shape coexistence phenomena.

Both experiments were performed at the ISOLDE facility at CERN. The radioactive ion beam that was produced by ISOLDE was implanted into a very thin carbon foil. Ten such carbon foils were mounted on a turnable wheel in the windmill chamber. Every supercycle, the wheel was turned, so that the foil, in which the beam was just implanted, is moved from the implantation station to the decay station. Four Si detectors were used to detect the fission fragments and the α particles: two at both sides of the foil at the implantation station, two at both sides of the foil at the decay station. A Miniball cluster detector with three Ge crystals, placed at the back of the windmill, behind the implantation station, was used to detect γ rays.

In the α-decay experiment, a substantial part of daughter nuclei ^{196}At recoiled back out of the foil. After correction factors were deduced for this recoil effect, an improved value of the EC/β^+-branching ratio of ^{196}At was obtained and compared with the tabulated value.

From the γ-ray study of ^{182}Tl, several features could be derived. In this thesis, the improved value of the half life of ^{182}Tl was deduced. Next, the $\gamma\gamma$-coincidence spectra are compared with each other to finally obtain the level scheme of ^{182}Hg. A strongly converted transition with an $E0$ component was observed between two mixed states with different deformation.

Contents

Chapter 1

Introduction

This chapter gives a general overview of the structure and decay properties of nuclei in the neutron-deficient Pb region in the vicinity of $N = 104$ mid shell. First, the nuclear shell model, deformation and shape coexistence are briefly described. Further, α, β, γ decay and β-delayed fission, are discussed. Finally, a short summary of previous studies of the α decay of ^{200}Fr and the β decay of ^{182}Tl is given. This chapter is mainly based on the book *Introductory Nuclear Physics* by S. Krane [Kra88]. Where there is made no other reference, tables, information and pictures were taken from this book.

1.1 Nuclear structure in the Pb region

Nuclei are represented by their number of protons Z and their number of neutrons N. A short notation ^{A}X is widely used, where X is the symbol of the chemical element determined by Z, and $A = Z + N$ is the mass number (number of nucleons). Nuclei with the same Z but different N are called isotopes. Likewise, nuclei with the same N are called isotones and with the same A isobars.

All four interactions are involved in an atomic nucleus. The nucleons are held together by the strong interaction. A repulsive force exists between the protons due to the electromagnetic interaction. The same interaction bounds the electrons to the nucleus. The weak interaction plays a role in the β decay of the nucleus. The gravitational interaction between the nucleons is negligible, with respect to the other interactions, due to extremely low masses ($m_{\mathrm{p}} \approx m_{\mathrm{n}} \approx 1.67 \times 10^{-27}\,\mathrm{kg}$ [Kra88]). Note that more than 99.9 % of the atomic matter is concentrated in the nucleus.

The mass of a nucleus does not equal to the sum of the masses of all nucleons. The nucleus has a reduced mass m_X due to the binding energy, generated by the strong interaction, which equals:

$$B = (Z m_{\mathrm{p}} + N m_{\mathrm{n}} - m_X)\, c^2 \ , \tag{1.1}$$

where m_{p} is the mass of the proton, m_{n} is the mass of the neutron and m_X is the mass of the whole nucleus. The binding energy of a nucleus depends on both the strong and electromagnetic force between the nucleons. Fig 1.1 gives the binding energy per nucleon B/A as a function of the mass number A.

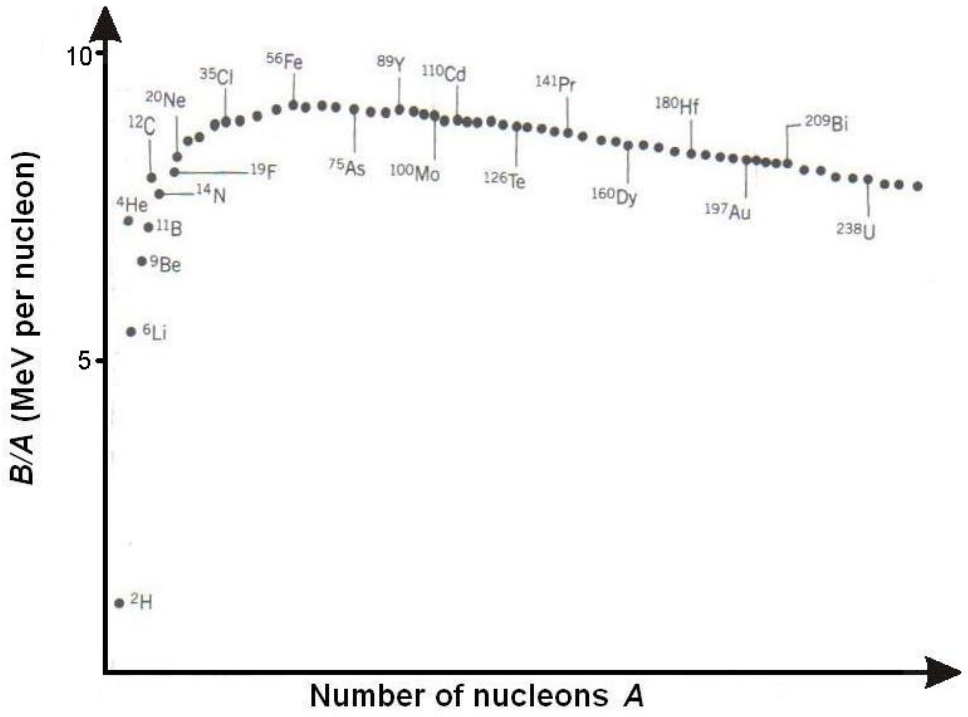

Figure 1.1: The binding energies per nucleon for different nuclei.

1.1.1 The Atomic Shell Model

Electrons move around the nucleons in a potential generated by the Coulomb interaction with the positively charged nucleus and between electrons. The wave functions of the electrons are solutions of the time-independent Schrödinger equation

$$-\frac{\hbar^2}{2m}\frac{d^2\psi}{d\overrightarrow{r}^2}(\overrightarrow{r}) + V(\overrightarrow{r})\psi(\overrightarrow{r}) = E\psi(\overrightarrow{r}) \tag{1.2}$$

where $V(\overline{x})$ is the spherical Coulomb potential which goes like $1/r$. Solutions for Eq 1.2 are wave functions with discrete energies

$$E_n = -\frac{mZ^2e^4}{32\pi^2\epsilon_0^2\hbar^2n^2}\ , \tag{1.3}$$

which are the eigenvalues of the Hamiltonian in Eq 1.2. For each level n, the permitted values for the orbital quantum number l of the electron are $0, 1, 2, \ldots, (n-1)$. The value for the magnetic quantum number m_l can vary from $-l$ to l. The energy levels with $n = 1, 2, 3, \ldots$ are called the K,L,M,... shells respectively.

An electron has an intrinsic spin either up or down ($m_s = \pm 1/2$). The wave function of an electron is completely defined by the discrete quantum numbers n, l, m_l and m_s. According to the Pauli principle, two identic fermions can never occupy a state with identical quantum numbers. Therefore, the K shell has the capacity to contain two electrons only, a first one with spin up, a second one with spin down, both having $l = 0$. The L shell can contain 8 electrons and so on. Lower shells are filled first, to form closed shells. This way, the atom has a core of closed shells and valence electrons in the outer shells. Most chemical and solid-state properties are explained by considering only valence electrons.

1.1.2 The Spherical Shell Model for Nucleons

A difference between electrons in atomic shells and nucleons in a nucleus, is that electrons move in an external potential, generated by the positive protons inside the nucleus, while the nucleons generate the potential themselves. Another problem is that the n-n, p-p and n-p interactions are not known exactly. One possibility to circumvent these problems, is the mean field approximation: every nucleon moves independently in an average potential caused by the other nucleons. If an infinite well or a harmonic oscillator is used for this average potential, the solution of the Shrödinger equation 1.2 gives energy levels like in Fig 1.2. Large gaps occur between some levels, which are associated with closed shells. The total number of nucleons at each shell closure are called magic numbers. Nuclei with a magic number of protons and neutrons are referred to as doubly-magic nuclei.

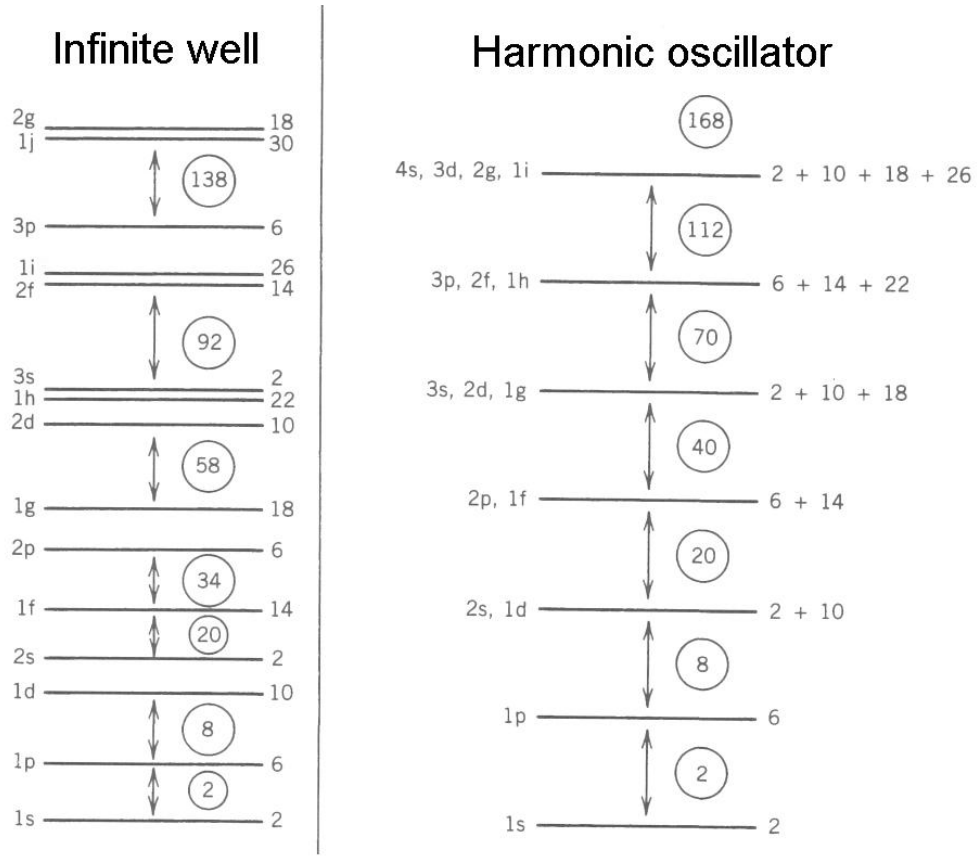

Figure 1.2: Shell structure for nucleons obtained with infinite well and harmonic oscillator potentials.

Magic numbers found by the infinite well or harmonic oscillator potential, which are given in Fig 1.2, do not agree with the experimentally observed magic numbers $2, 8, 20, 28, 50, 82$ and 126, see Fig 1.3.
The infinite well potential is to sharp, the harmonic oscillator not sharp enough. Instead of them, the more realistic Woods-Saxon potential

$$V(r) = \frac{-V_0}{1 + \exp[(r - R)/a]} \tag{1.4}$$

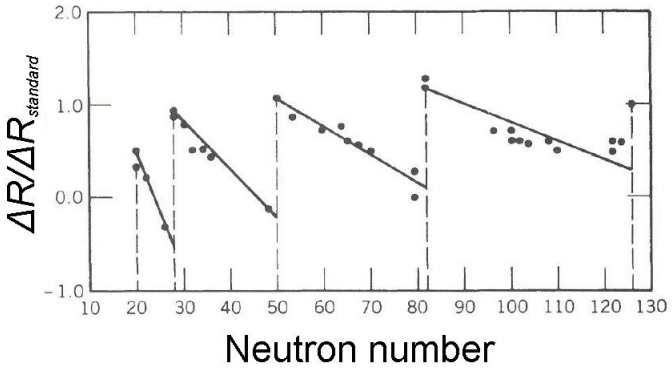

Figure 1.3: Evidence for the nuclear shell structure: Change in the nuclear charge radius when $\Delta N = 2$. Sudden jumps occur at $N = 20, 28, 50, 82$ and 126, which are magic numbers (in addition, 2 and 8 are also magic numbers). ΔR is normalized to $\Delta R_{standard} \sim A^{1/3}$.

is widely used. If the spin-orbit interaction $\langle \overrightarrow{l}, \overrightarrow{s} \rangle$ is added to the Woods-Saxon potential [May49], proper magic numbers are obtained by solving the Schrödinger equation, see Fig 1.4.

The spin-orbit interaction is represented by the quantum number $\mathbf{j} = \mathbf{l}+\mathbf{s}$, the total angular momentum. Since $s = 1/2$, the possible values for j are $l \pm 1/2$. The wave function of a nucleon is completely defined by the quantum numbers l (=0,1,2,...), s (=1/2), j ($=l\pm1/2$) and m_j ($=-j, -j+1, ..., j-1, j$). The intrinsic spin of a nucleon is always 1/2, so this quantum number is often not explicitly mentioned. The index n counts the number of levels with a certain orbital number l. States with the same index n and the same quantum numbers l and j are degenerate. They are written in short-hand notation as nx_j, where $x = s, p, d, f, ...$ for $l = 0, 1, 2, 3, \ldots$ respectively. For example, $2p_{3/2}$ represents the second orbital with $l = 1$ and $j = 1 + 1/2$, which can contain 4 nucleons. The parity of a state equals $(-1)^l$.

Most properties of nuclei close to doubly-magic nuclei are described well by considering only the valence nucleons or the holes in the closed-shell core. Far away from the doubly-magic nuclei, this simple representation does not hold anymore.

Nucleus ^{200}Fr consists out of 87 protons and 113 neutrons. Protons fill shells up to magic number 82. The remaining 5 protons can be in the $1h_{9/2}$, $1i_{13/2}$ or even higher-lying states. 112 neutrons can have a two hole configuration in the $1i_{13/2}$ shell.

Nucleus ^{182}Tl consists out of 81 protons and 101 neutrons. It has one proton short of having a magic number of protons. The protons have a one-hole configuration in shell $3s_{1/2}$. 82 neutrons fill the closed shell with magic number 82. The other 19 neutrons can have for example a $8\times2f_{7/2}$,$10\times1h_{9/2}$,$1i_{13/2}$ configuration. For this configuration, the proton hole with $j_\pi = 1/2$, negative parity, and the valence neutron with $j_\nu = 13/2$, negative parity, could couple to a total $J = 6, 7$ with positive parity. This is only one possibility, other configurations can also occur, and experiments can indicate which configuration is the ground state of the nucleus.

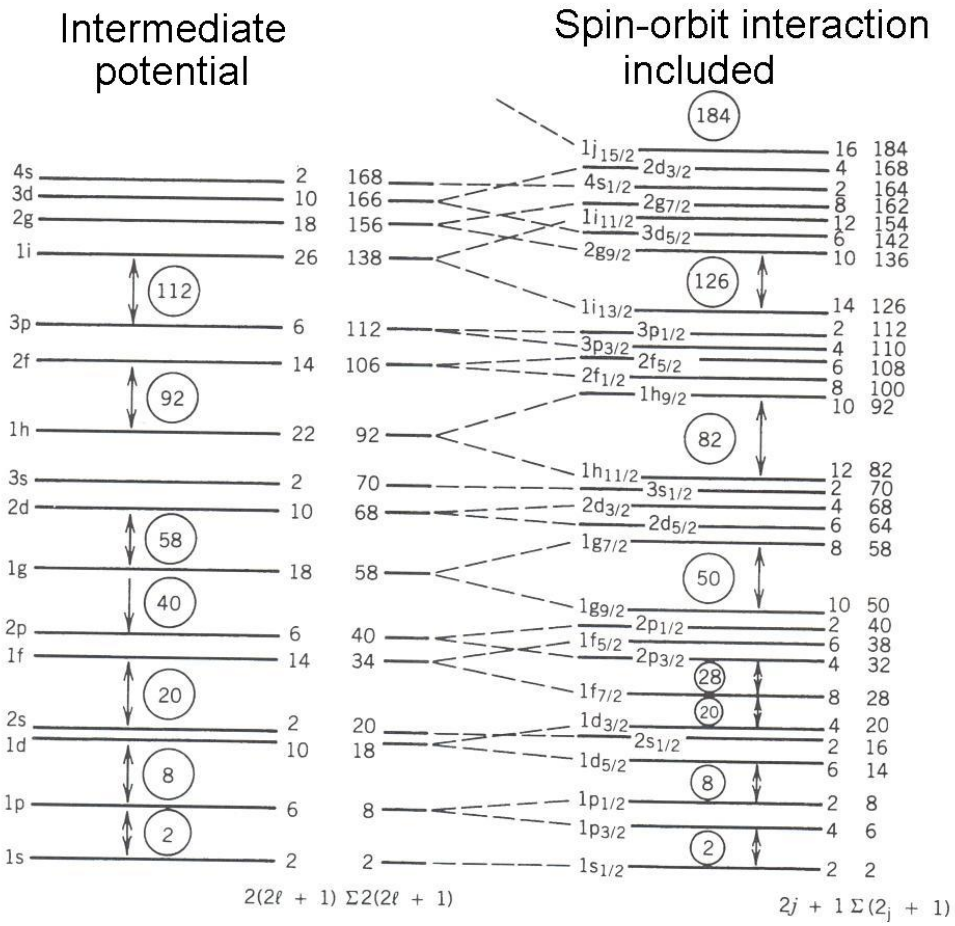

Figure 1.4: Shell structure for nucleons when calculated by (left) the Woods-Saxon potential (Eq 1.4) and (right) including the spin-orbit interaction.

1.1.3 Deformed nuclei and nuclear rotations

As discussed above, the Spherical Shell Model is based on the assumption that the nucleons move in a spherical central potential. However this approach can not be used for nuclei in the range $150 \leq A \leq 190$ and $A > 230$. The nuclei in this range can have a prolate or oblate ellipsoid shape (Fig 1.5). The deformation is characterized by the deformation parameter β, which is related to the eccentricity of the ellipse as

$$\beta = \frac{4}{3}\sqrt{\frac{\pi}{5}}\frac{\Delta R}{R_{\text{av}}}\,, \tag{1.5}$$

where $\Delta R = R_{\text{sym}} - R_{\perp}$ is the difference between the radius in the direction of the symmetry axis and the radius in a direction perpendicular to the symmetry axis, see Fig 1.5. R_{av} is the average radius of the nucleus. If $\beta > 0$, the nucleus has the form of a prolate ellipsoid (rugby ball shape). If $\beta < 0$, the nucleus has the form of an oblate ellipsoid (discus shape).

Deformed nuclei can rotate around an axis perpendicular to the symmetry axis of the nucleus. When the nucleus is considered to be a ridged body, the energy of a rotating

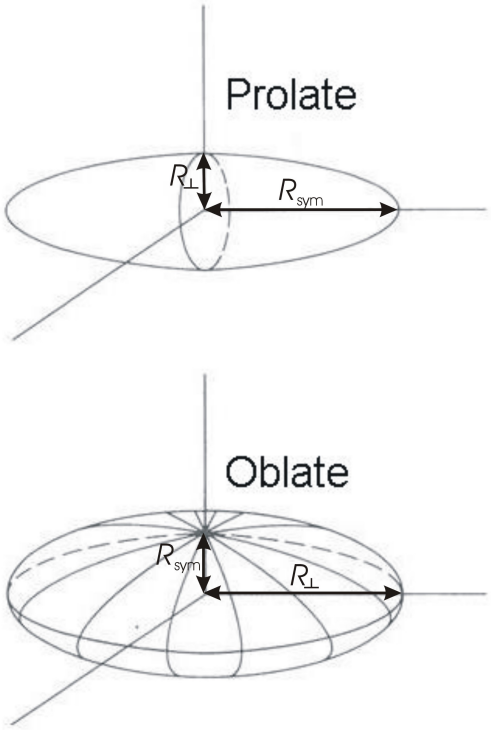

Figure 1.5: A prolate (top) and oblate (bottom) ellipsoid. The differences $\Delta R = R_{\text{sym}} - R_\perp$ are exaggerated to clearly visualize the two shapes.

nucleus is given by

$$E = \frac{\hbar^2}{2\mathfrak{I}} I(I+1) \tag{1.6}$$

with I representing the angular momentum of the rotating nucleus, and $\mathfrak{I}$ the static moment of inertia. The excited states form a rotational band, which is the sequence of states with spins I, $I+1$, $I+2$,... where I is the spin of the lowest state, called the band head. In some cases, a nucleus has two or more possible deformations, each with their own rotational band. Note that for a 0^+ band head only even values of I are possible.

The ratios

$$E(4^+)/E(2^+) = 3.33$$
$$E(6^+)/E(4^+) = 2.1$$
$$E(8^+)/E(6^+) = 1.71$$

for even-N, even-Z nuclei, which have a 0^+ ground state, are in good agreement with experimentally observed ratios in the rotational bands.

The Nilsson model takes the rotation of the nucleus into account, when solving the Schrödinger equation 1.2. The eigenvalues in the Nilsson model give the energy levels of the single particles in deformed nuclei, as a function of the deformation parameter β.

In Fig 1.7, the solutions of the Nilsson model, for $Z \geq 82$, are presented. When the deformation parameter β=0, the nucleus can not rotate and the Hamiltonian becomes the same as in the spherical model.

As shown in the Nilsson diagram in Fig 1.7, the Nilsson state 1/2[660], arising from the $1i_{13/2}$ shell, is lowering in energy when the deformation parameter is becoming larger. This results in two low lying nuclear states having a different shape: one spherical (1/2[400]) and one prolate (1/2[660]). This effect is referred to as shape coexistence. Because in this example, the two states have the same spin and parity, the two states are mixed.

1.1.4 Two-state mixing

Consider two nuclear states with the same spin and parity, wave functions φ_1, φ_2 and energies E_1, E_2, see Fig 1.6. These pure configurations are seldom encountered, mostly the nuclear states are complex mixtures of pure components [Cas90]. For an interaction potential V, the mixed states ψ_{I} and ψ_{II} and their energies are obtained by diagonalizing the 2×2 matrix

$$\begin{pmatrix} E_1 & V \\ V & E_2 \end{pmatrix}$$

so the final nuclear states depend on both ΔE_{pure} and the interaction strength. The solution for the mixed wave functions are

$$\begin{aligned} \psi_{\mathrm{I}} &= a\varphi_1 + b\varphi_2 \\ \psi_{\mathrm{II}} &= -b\varphi_1 + a\varphi_2 \end{aligned} \tag{1.7}$$

where $a^2 + b^2 = 1$ and the smaller amplitude b is given by

$$b = \frac{1}{\left(1 + \left[\frac{\Delta E_{pure}}{2V} + \sqrt{1 + \left(\frac{\Delta E_{pure}}{2V}\right)^2}\right]^2\right)^{1/2}} \quad . \tag{1.8}$$

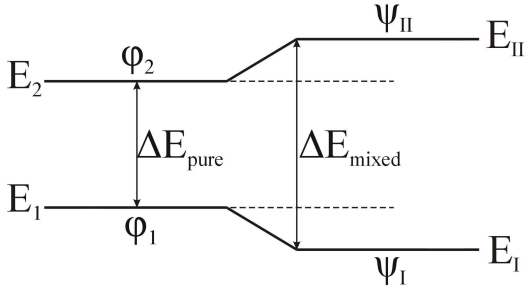

Figure 1.6: Two-state mixing between φ_1 and φ_2, with the same spin and parity [Cas90].

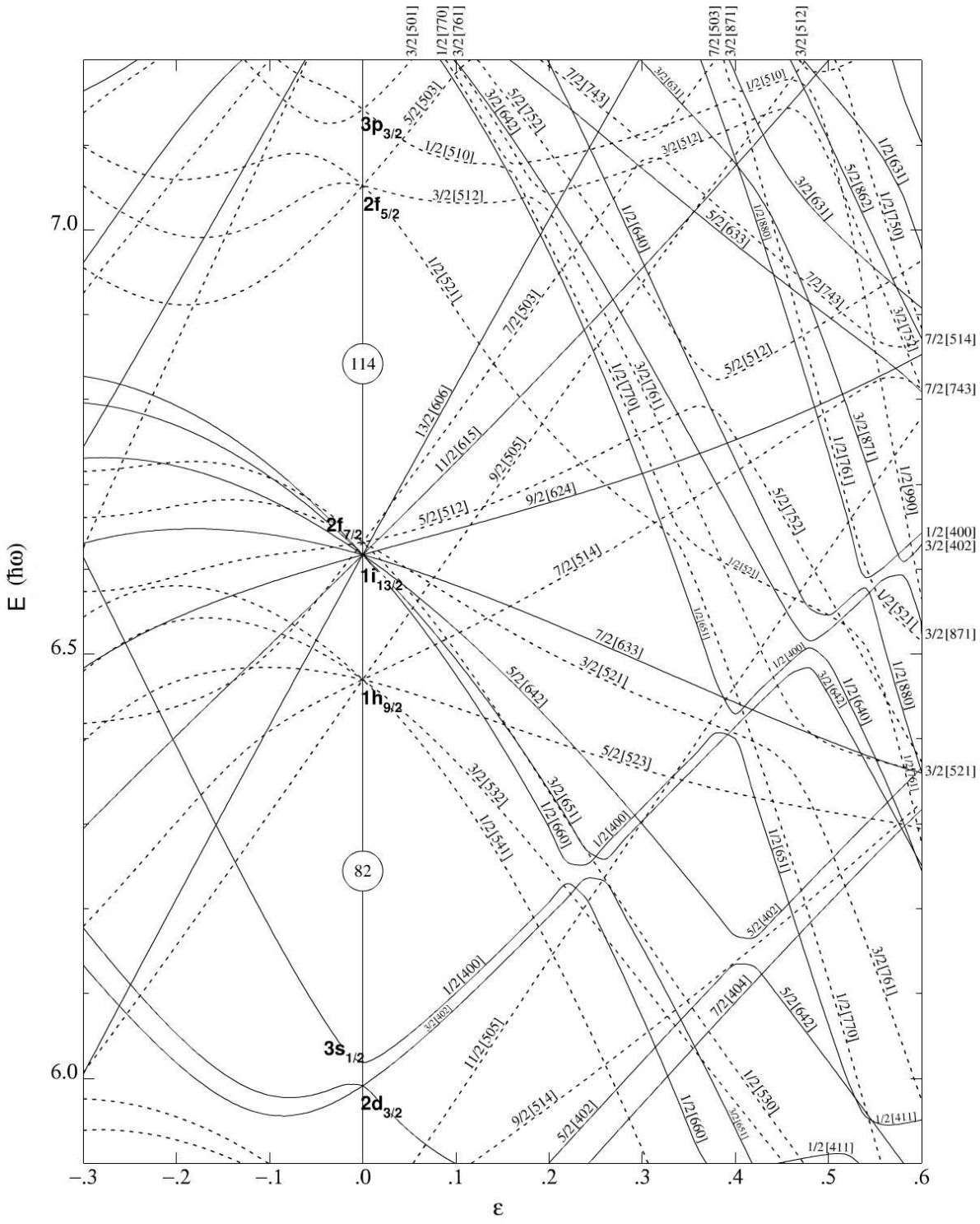

Figure 1.7: Nilsson diagram for protons, $Z \geq 82$: The splitting of levels with the same j and different m_j, is due to the deformation which lifts the symmetry in the nucleus. ϵ is a deformation parameter, related to β. The figure was adapted from [Fir99].

1.2 Decay modes in the Pb region

On the nuclear chart in Fig 1.8, all known nuclei are indicated as a function of Z and N. The black squares represent the stable nuclei. Together they are called the β-stability line. The colored squares represent the different decay modes of the nuclei: α decay, EC/β^+ decay, β^- decay, proton emission, neutron emission and spontaneous fission. The very neutron-deficient Pb region is far from the line of stability. Therefore nuclei in this region have very high Q values and different modes of decay are accessible, namely α and EC/β^+ decay. These decay modes are discussed in the next sections (Fig 1.9).
Nuclei on the left-hand side of the line of stability are so called neutron-deficient nuclei, because they have less neutrons with respect to their stable isotopes. Likewise, nuclei to the right of the line of stability are referred as neutron-rich nuclei.

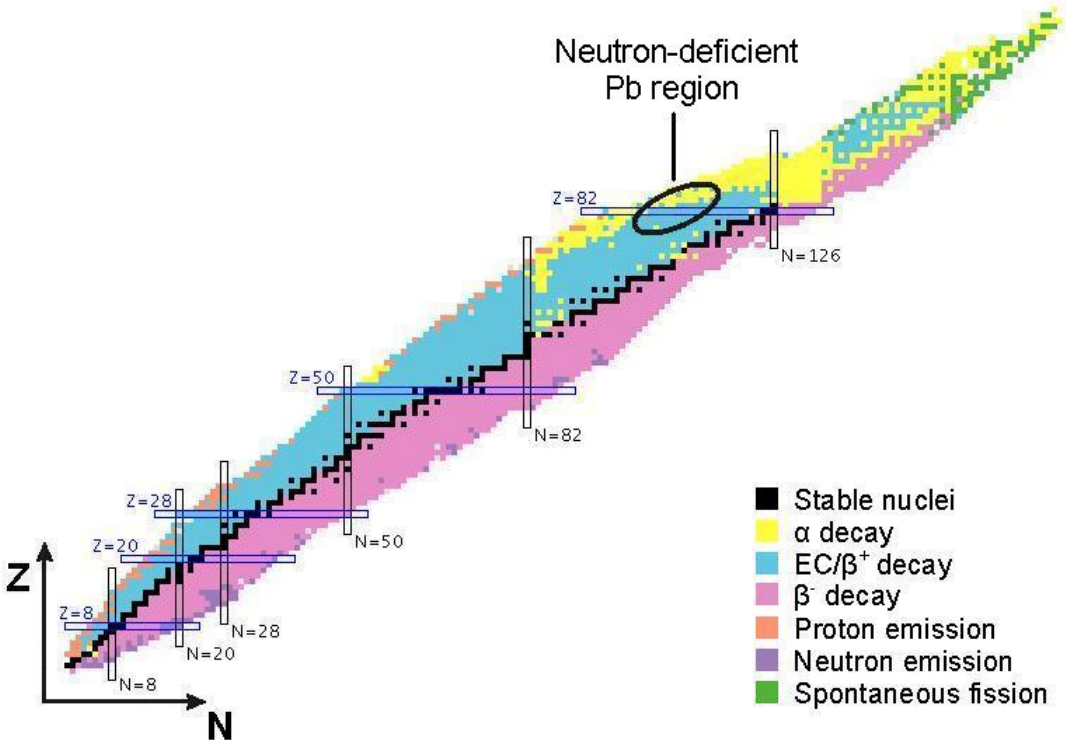

Figure 1.8: The Nuclear Chart [Nat10]. Different colors represent different decay modes. Nuclei with magic proton or neutron numbers are indicated.

1.2.1 α decay

The α decay is a process where the nucleus emits an α particle which consist out of 2 protons and 2 neutrons. It is the strong and electromagnetic interaction that is responsible for α decay. The α decay can be schematically represented as

$$ {}^{A}_{Z}X_N \rightarrow {}^{A-4}_{Z-2}Y_{N-2} + \alpha. $$

The Q value is defined as the energy released in the decay, in the form of kinetic energy of the decay products. The Q value for α decay, from the ground state of the parent nucleus

X, to the ground state of the daughter nucleus Y is given by the difference between the masses of the initial and final nuclei,

$$Q = (m_X - m_Y - m_\alpha)c^2 \ , \tag{1.9}$$

where m_X, m_Y and m_α are the masses of the correspondent nuclei and c is the speed of light. Only when $Q > 0$, α decay can occur spontaneously. The daughter nucleus can be in excited state Y^*, the mass of the excited state is denoted by m_{Y^*}.

The Q value for α decay in the Pb region of interest is typically of the order of 5 MeV. According to the Geiger-Nuttall rule, the $\log(fT_{1/2})$ value is linearly dependent on the Q value.

The rate of which states of the daughter nucleus are populated, depends on the wave functions of the initial and final states:

- the larger the change in angular momentum between the initial and final state, the smaller the intensity to populate the final state and vice versa;
- it is forbidden to have parity change between the initial and final states.

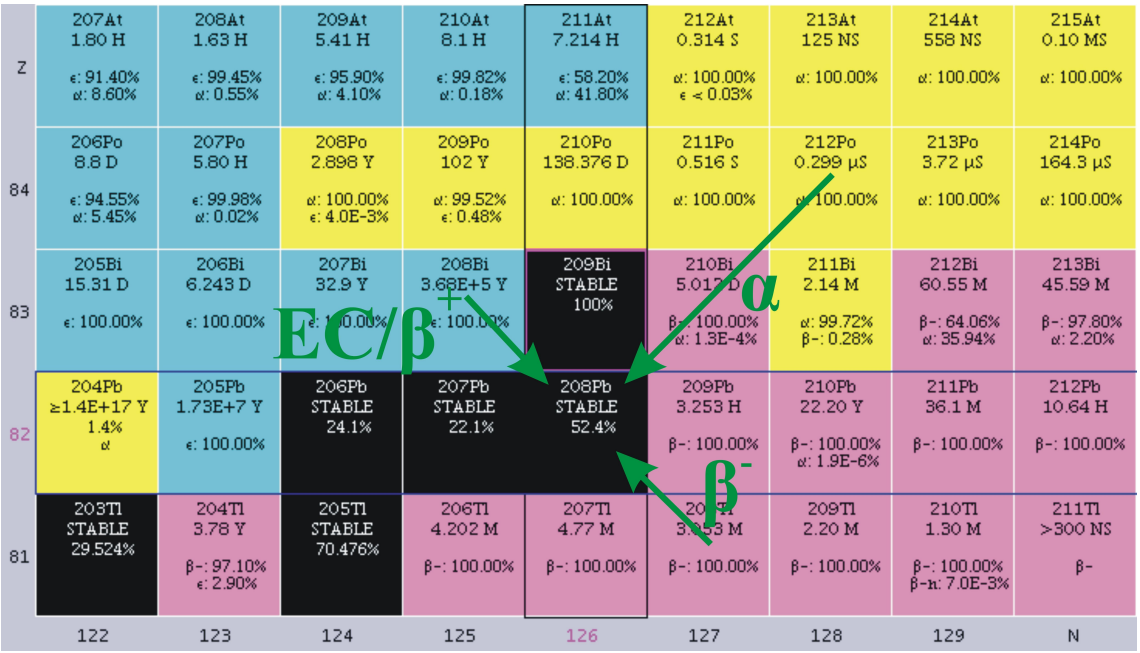

Figure 1.9: Representation of the α and β decay modes on the nuclear chart [Nat10].

Conservation of momentum and energy in the α decay process gives the equations:

$$m_X v_X = m_\alpha v_\alpha + m_Y v_Y \quad \textit{and} \tag{1.10}$$

$$\frac{m_X v_X^2}{2} = \frac{m_\alpha v_\alpha^2}{2} + \frac{m_Y v_Y^2}{2} - Q \tag{1.11}$$

If the decaying nucleus is at rest, the energies of the decay products are uniquely defined.

1.2.2 β decay

There are three types of β decay: β^-, β^+ and electron capture (EC). These three types of decay are grouped together because they all occur due to the electro-weak interaction.

β^- decay is a process whereby one neutron of the nucleus is converted into a proton, together with the emission of an electron and an antineutrino, schematically:

$$\begin{aligned} \mathrm{n} &\rightarrow \mathrm{p} + \mathrm{e}^- + \overline{\nu}_\mathrm{e} \ , \\ {}^{A}_{Z}X_N &\rightarrow {}^{A}_{Z+1}Y_{N-1} + \mathrm{e}^- + \overline{\nu}_\mathrm{e} \ . \end{aligned}$$

The Q value for β^- decay is

$$Q_{\beta^-} = (m_X - m_Y)c^2 \tag{1.12}$$

where m_X and m_Y equal to the masses of the correspondent atoms. The mass of the emitted electron does not appear in this formula, because it is included in the atomic mass of Y. The β^- decay process only occurs in nuclei in the neutron-rich region of the nuclear chart.

β^+ decay is a process whereby one proton of the nucleus is converted into a neutron, along with the emission of a positron and a neutrino:

$$\begin{aligned} \mathrm{p} &\rightarrow \mathrm{n} + \mathrm{e}^+ + \nu_\mathrm{e} \ , \\ {}^{A}_{Z}X_N &\rightarrow {}^{A}_{Z-1}Y_{N+1} + \mathrm{e}^+ + \nu_\mathrm{e} \ . \end{aligned}$$

For the Q value of β^+ decay to the ground state, the mass of the electron m_e needs to be taken into account twice: once for the excess electron in the Y atom and a second time for the positron, therefore:

$$Q_{\beta^+} = (m_X - m_Y - 2m_\mathrm{e})c^2 \ . \tag{1.13}$$

The positron will subsequently annihilate with an electron and two γ rays of 511 keV are emitted back-to-back. The β^+ decay is typical for neutron-deficient nuclei.

When a nucleus decays by electron capture (EC), an electron of one of the atomic shells interacts with a proton in the nucleus resulting in a neutron. The electron must have a non-zero probability to be found inside the nucleus, therefore the electron is usually in the K shell, less probable in the L shell. A neutrino is emitted during the decay:

$$\begin{aligned} \mathrm{p} + \mathrm{e}^- &\rightarrow \mathrm{n} + \nu_\mathrm{e} \ , \\ {}^{A}_{Z}X_N &\rightarrow {}^{A}_{Z-1}Y_{N+1} + \nu_\mathrm{e} \ . \end{aligned}$$

The Q value for EC is defined as

$$Q_\mathrm{EC} = (m_X - m_Y)c^2 - B_\mathrm{e} \tag{1.14}$$

where B_e is the binding energy of the captured electron. The vacancy in the K or L shell of the daughter atom is filled by other electrons. This results in the emission of characteristic X rays or Auger electrons. EC is also a decay mode that occurs for nuclei in the neutron-deficient region and is a competitive process of β^+ decay.

All β decay modes transform the parent nucleus into a nucleus with the same number of nucleons A, closer to the line of stability. This thesis concerns the decay study of nuclei in the neutron-deficient Pb region. In this region, no β^- decay occurs, β^+ and EC decay are competitive processes to α decay.

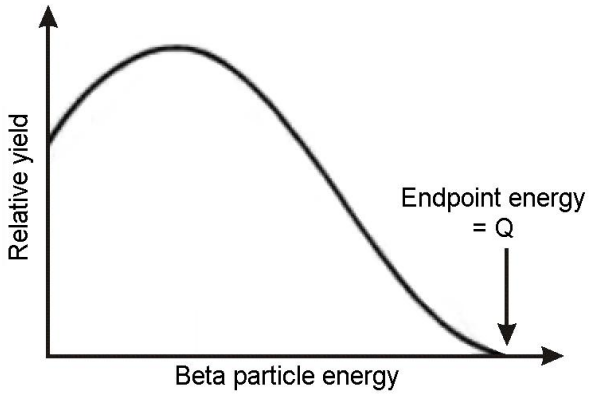

Figure 1.10: Typical continuous energy distribution of a β^+ particle. The figure was adapted from [Kno99].

The kinematic laws for conservation of momentum and energy apply. The radioactive nuclei in the experiments, discussed in the present thesis, are at rest at the moment of their decay. Therefore the initial momentum and energy, p_X and E_X, equal to zero. The sum of the kinetic energies of all decay products equals the Q value. EC has a two-body final state. The conservation laws for EC decay become

$$m_Y v_Y + m_\nu v_\nu = 0 \quad \text{and} \tag{1.15}$$

$$\frac{m_Y v_Y^2}{2} + \frac{m_\nu v_\nu^2}{2} = Q \tag{1.16}$$

Therefore the neutrino and the daughter nucleus have a well defined kinetic energy. The β^+ decay has three decay products. For this reason, the positron has a continuous energy distribution with an endpoint energy equal to the Q value, as depicted in Fig 1.10.

The Q value of EC, determined by Eq 1.14, is higher than that of β^+ decay, from Eq 1.13, since with the latter energy is needed to create a positron. Probabilities for a nucleus to decay by emitting a β^+ particle or by EC, strongly depends on the Q value. In some cases, it is possible that EC can occur ($Q > 0$) while β^+ decay is prohibited ($Q < 0$). Fig 1.11 shows that high energy states of the daughter nuclei are mainly populated by EC decay, while low energy states are mainly populated by β^+ decay.

The probability and half life of β decay depend strongly on the difference in spin ΔI and on the change in parity between the parent and the daughter nucleus. The β decay where ΔI equals to 0 or 1 and where there is no parity change, is the most probable and is called allowed β decay. When an allowed decay is not possible, for example when parity change

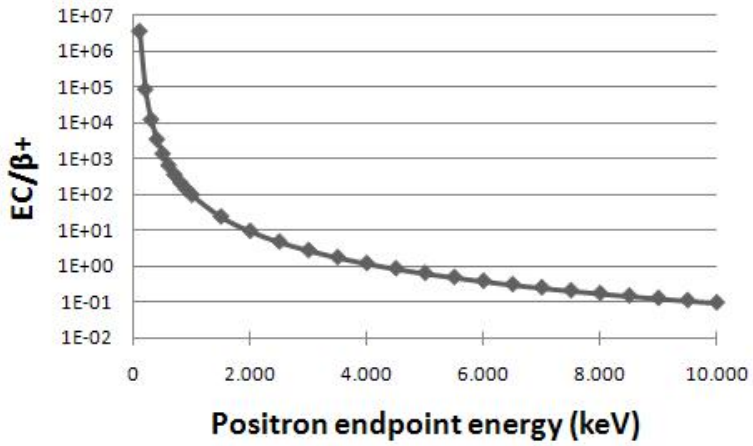

Figure 1.11: The EC/β^+-branching ratio in function of the endpoint energy of the positron (Q value) for ^{182}Tl$\rightarrow^{182}$Hg.

is involved, a forbidden decay can be observed. A forbidden decay has a lower probability then the allowed decay. A first-forbidden decay involves a transition with $\Delta I = 0, 1, 2$ and parity change. The second-forbidden decay has a $\Delta I = 2, 3$ and no parity change and so on for higher orders. Each forbidden decay with a higher order becomes less probable. That is why forbidden decays solely can be observed if they are the only possible decay modes.

1.2.3 Electromagnetic processes

After α or β decay, the daughter nucleus can be in an excited state with energy E^*. The excited nucleus can subsequently deexite through γ emission. The excess of energy can also be carried away by emitting one of the electrons from a atomic shell through the internal conversion process.

γ rays

Conservation of impulse imposes that the nucleus recoils while emitting a γ ray. Typically, this recoil energy is about a factor 10^{-5} of the energy difference between the initial and final nuclear state, therefore it is often neglected. Thus, the γ ray has an energy equal to the energy difference between these two states.

The difference in angular momentum between the two states is transmitted by the angular momentum $L\hbar$ of the γ ray. Angular momentum must be conserved. The initial angular momentum, $\overrightarrow{J_i}$, must be equal to the total angular momentum after γ decay, $\overrightarrow{J_f} + \overrightarrow{L}$. Via quantum mechanics, the angular momentum selection rule is

$$|J_i - J_f| \leq L \leq J_i + J_f \ .$$

The γ ray can be of electrical or magnetic character and its parity is:

$$\begin{aligned} \pi(EL) &= (-1)^L \qquad \text{and} \\ \pi(ML) &= (-1)^{L+1} \quad . \end{aligned}$$

The electric transitions are related to the charge distribution in the nucleus, while the magnetic ones to electric fluxes inside the nucleus. Emission of a γ ray with $L = 0$ is strictly forbidden, since the intrinsic spin of photons equals to 1.

The Weisskopf estimates give the probability for electric or magnetic transition, as a function of the multipolarity, the energy and the mass number A. The probability decreases fast with increasing multipolarity. In most cases, the probability increases with the energy of the transition and the mass number A of the nucleus. For the same multipolarity, the probability for electric transitions is higher than for magnetic transitions. Therefore, in the case of magnetic transitions, the possibility of admixtures of an electric transition of higher order needs to be considered. The main multipolarities of the γ particle in function of the parity and the angular momentum change are shown in the table below.

ΔJ	**0**	**1**	**2**	**3**	**4**
$\pi_i\pi_f =$ **-1**	$E1$	$E1$	$M2/E3$	$E3$	$M4/E5$
$\pi_i\pi_f =$ **+1**	$M1/E2$	$M1/E2$	$E2$	$M3/E4$	$E4$

For transitions from 0^+ to 0^+, the angular momentum selection rule states that $L = 0$. Since this is forbidden, no γ ray can be emitted during a $0^+ \rightarrow 0^+$ transition. Therefore other decay modes must be considered.

Internal conversion

Internal conversion (IC) is a competing electromagnetic process of γ-ray emission. The nucleus transfers its excitation energy to an electron in one of the inner atomic shells. The electron can then escape from the atom with kinetic energy:

$$T_\mathrm{e} = \Delta E - B_\mathrm{e} \ , \tag{1.17}$$

where ΔE is the difference in energy between two nuclear states and B_e is the binding energy of the electron in the atomic shell. Different atomic shells, have different binding energies. After IC, there is an electron vacancy left in the atom, which results in other electrons filling the vacancy. Characteristic X rays and/or Auger electrons are emitted during this process.

The internal conversion coefficient ICC is defined as the ratio of the probability of IC λ_e to the probability of γ-ray emission λ_γ,

$$ICC = \frac{\lambda_e}{\lambda_\gamma} \ . \tag{1.18}$$

The ICC is sensitive to the transition multipolarity. Therefore it is often used to determine the multipolarity of transitions.

The internal conversion coefficient increases as Z^3, so it becomes important in the Pb region. The conversion coefficient also increases with the multipolarity of the transition, because the probability for γ decay decreases. The conversion coefficient decreases rapidly with increasing transition energy. For $0^+ \rightarrow 0^+$, γ-ray emission is forbidden, only IC is possible and the transition is fully converted.

$E0$ transitions as a fingerprint of two-state mixing

$E0$ transitions not only occur in $0^+ \rightarrow 0^+$ decay, but can also be a component in a $I^\pi \rightarrow I^\pi$ (equal spin and parity with $I > 0$) transitions. There is evidence that the strength of an

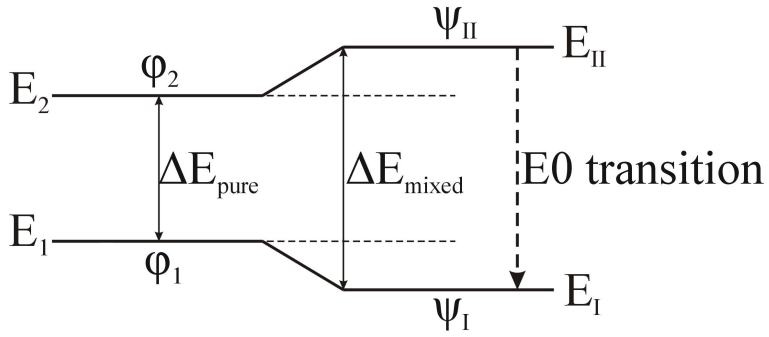

Figure 1.12: Two-state mixing between φ_1 and φ_2, with the same spin and parity [Cas90].

$E0$ transitions is associated with the mixing of initial and final states and with the shape coexistence [Kan84]. The strength of an $E0$ transition $\rho^2(E0)$ can be expressed as

$$\rho^2(E0) \sim a^2 b^2 (\Delta\langle\beta^2\rangle)^2 \ , \tag{1.19}$$

where a and b are the mixing amplitudes, see Eq 1.7, and $\Delta\langle\beta^2\rangle$ is the difference in quadrupole deformation of initial and final states. Thus, **the observation of $E0$ transition, which is determined by measuring the ICC, allows to draw the conclusion that the initial and final state have the same spin and parity, are mixed and moreover have a difference in their deformation.**

1.2.4 β-delayed fission

The binding energy per nucleon, B/A, is depicted in Fig 1.1. The binding energy per nucleon for nuclei with $A > 56$ decreases with the number of nucleons which leads to the fact that the possibility of generating energy by the fusion of two light nuclei, stops around that number. Conversely, for heavier nuclei, it becomes possible to generate energy by splitting a heavier nucleus in lighter fragments.

However, the competition between the strong force and the Coulomb force generates a fission barrier B_F, which keeps the two fragments together. In most of the nuclei, this fission barrier is too high to have a substantial fission branch. For some heavy nuclei ($A > 250$), this fission barrier becomes so small that the probability to fission becomes important. The penetration through the barrier is called tunneling. This decay process is known as spontaneous fission (Fig 1.13a).

After β decay of the parent nucleus, the daughter nucleus can be in an excited state. If the energy E^* of this excited state is comparable to or higher than the fission barrier, the nucleus can decay through fission (Fig 1.13b). Half lives for β decay are typically longer than a couple of milliseconds, while fission after β decay occurs within less then a nanosecond. It follows that this kind of fission is observed with the half life of the β decay of the parent nucleus and therefore the process is called β-delayed fission.

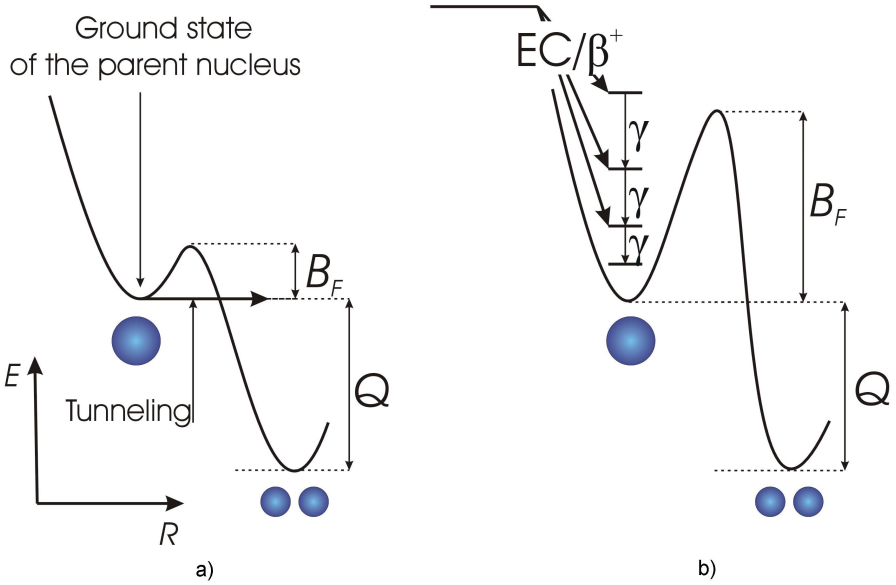

Figure 1.13: Schematic representation of a) spontaneous fission and b) β-delayed fission, R is the separation distance between the two fragments.

The probability of β-delayed fission, $P_{\beta DF}$, is defined as the ratio between the number of observed βDF events $N_{\beta DF}$ to the number of β decays N_β:

$$P_{\beta DF} = \frac{N_{\beta DF}}{N_\beta} \ . \tag{1.20}$$

$P_{\beta DF}$ is strongly dependent of the fission barrier B_f. Therefore it provides a unique tool to study fission barriers in exotic nuclei.

To study βDF carefully, the branching ratios and Q_{EC} of the parent nucleus and the nuclear structure of both parent and daughter nuclei, are needed. In the first part of the present thesis, the branching ratios of the decay of ^{196}At were determined by investigating the α-decay chain ^{200}Fr$\rightarrow^{196}$At$\rightarrow^{192}$Bi. In the second part, the nuclear structure of ^{182}Tl and ^{182}Hg was investigated by studying the γ rays subsequent to the β decay of ^{182}Tl.

1.3 Decay of ^{200}Fr

The heavy nucleus ^{200}Fr has 87 protons and 113 neutrons. It decays for 100 % via α emission to the ground state ^{196}At, with a half life $T_{1/2}$=49(4) ms and a Q value of 7621(50)keV [Nat10]. The decay scheme of ^{200}Fr and its decay products is given in Fig 1.14. ^{196}At ($T_{1/2}$ = 388(7) ms [Fir99]), which is the daughter nucleus of ^{200}Fr, decays either via α emission to ^{192}Bi, or via EC/β^+ decay to ^{196}Po. Just recently [And], a small β-delayed fission branch was discovered in ^{196}At. Fig 1.14 indicates that to obtain the probability for βDF, it is important to know the branching ratio between α and EC/β^+. The first part of the present thesis concentrates on determining this branching ratio for the nucleus ^{196}At.

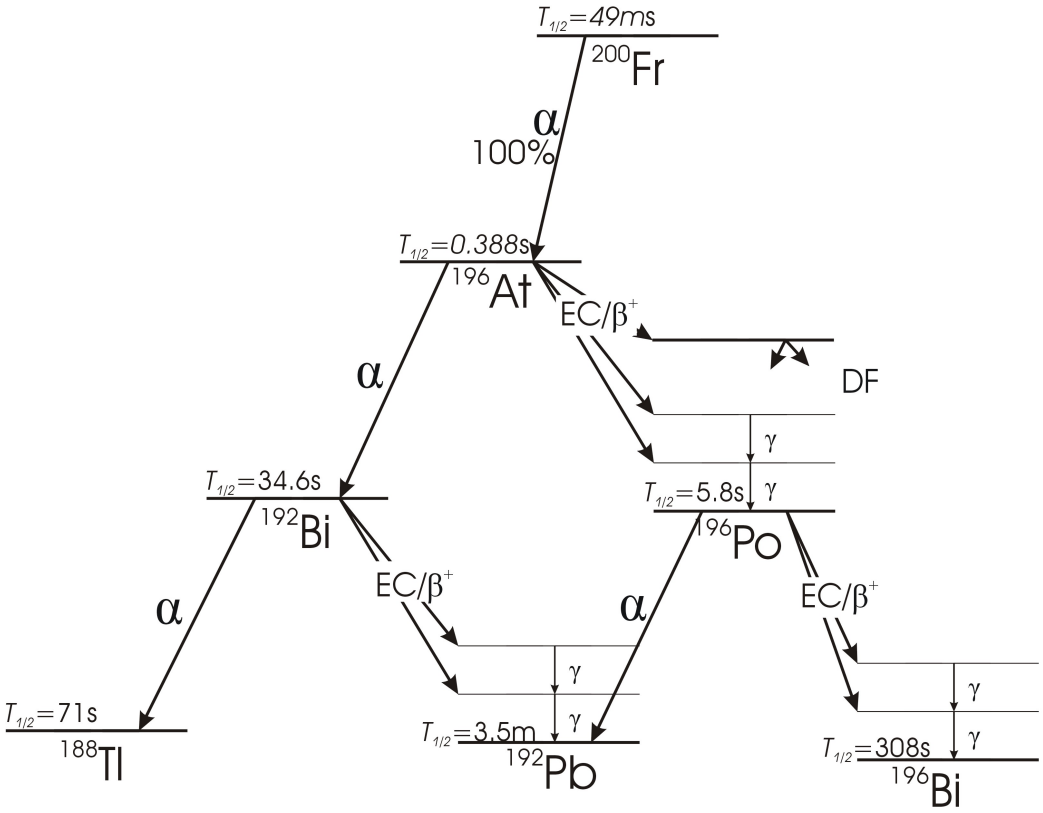

Figure 1.14: Scheme of the decay cascade of nucleus ^{200}Fr. The half life and decay modes are given for each nucleus [Nat10].

1.3.1 Previous studies of the α decay of ^{200}Fr

In 2005, an article was published by H. De Witte and others, about the α decay of neutron deficient ^{200}Fr and heavier neighbors [Wit05]. The experiment was carried out at the ISOLDE facility at CERN. A half life for ^{200}Fr of 49(4)ms has been obtained and an α-branching ratio of 94(5)% for the decay of ^{196}At.

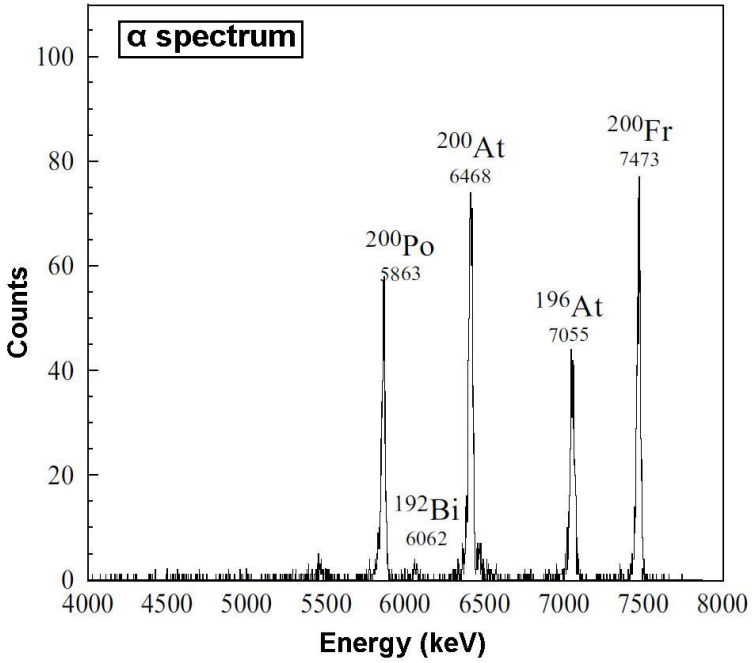

Figure 1.15: The α spectrum recorded at A=200. The energy and origin of each peak are indicated. The picture was adapted from [Wit05].

1.4 Decay of ^{182}Tl

The very neutron-deficient nucleus ^{182}Tl, consists of 81 protons and 101 neutrons. The main decay mode (96 %) is EC/β^+ decay to ^{182}Hg. There is a probability of less then 4 % that the nucleus will decay to ^{178}Au by α emission [Ach09]. The daughter nucleus ^{182}Hg also decays mainly by EC/β^+ decay [Fir99]. The decay chain of ^{182}Tl is given in Fig 1.16.

The energy of the excited daughter nucleus ^{182}Hg*, fed by EC/β^+ decay, can be up to 10 Mev, which is the difference between binding energies of ^{182}Tl and ^{182}Hg [Nat10]. This energy is comparable to the height of the fission barrier of ^{182}Hg, therefore β-delayed fission is expected [Laz87].

The βDF has to compete with electromagnetic decay. The second part of the present thesis concentrates on the γ decay after EC/β^+ decay of ^{182}Tl.

1.4.1 Previous studies of ^{182}Hg

Recently, the Coulomb excitation of light Hg nuclei has been performed at REX, ISOLDE. The experiment showed that the lowest 4^+ state of ^{182}Hg is a level of a different rotational band than the lowest 2^+ state [Pet08].

The in-beam experiment which was performed in the Gammasphere Array at ANL, revealed a complex level scheme of ^{182}Hg, which is shown in Fig 1.17 [Bin95]. ^{182}Hg was formed by impinging a beam of ^{32}S on a ^{154}Gd target. The yrast rotational band 4 in Fig 1.17, which was presumably assigned as a deformed intruder band, was observed up to spin 20^+.

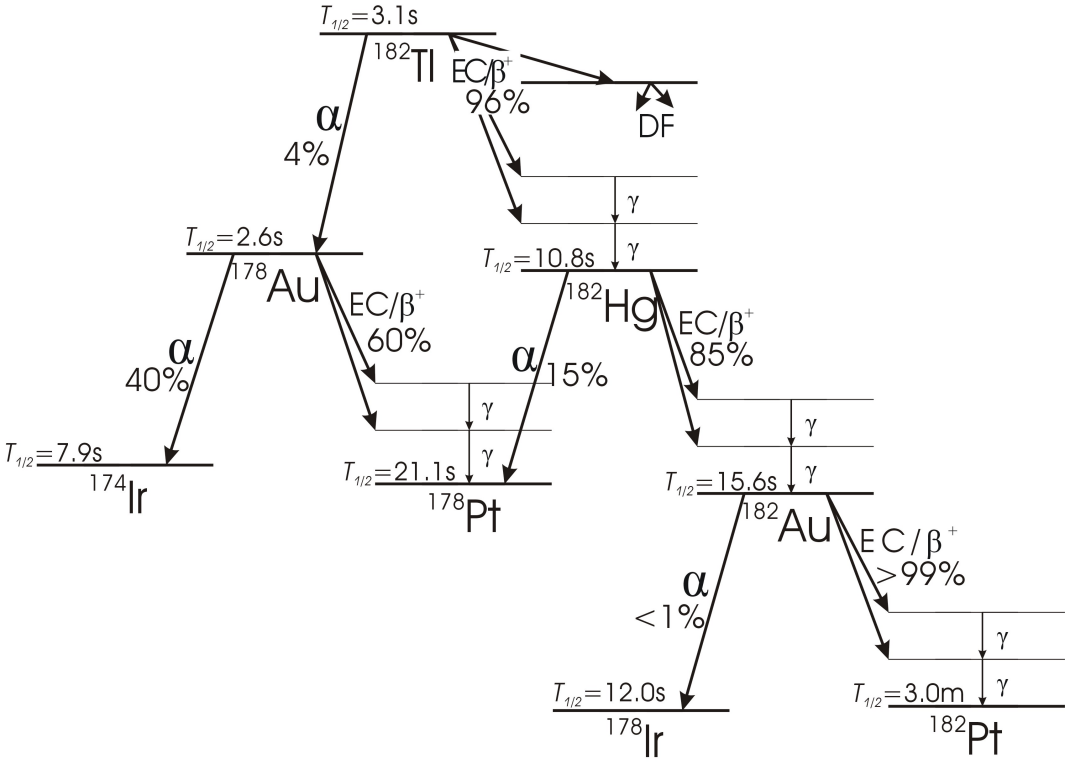

Figure 1.16: Scheme of the decay cascade of nucleus ^{182}Tl. The half life, decay modes and branching ratios are given for each nucleus [Nat10].

Previously a short note on ^{182}Tl β^+/EC decay was published [Bou91]. In the article, a half life $T_{1/2}$ of 3.1(10) s is reported for ^{182}Tl. Four γ transitions from the daughter nucleus ^{182}Hg, corresponding to the $8^+ \to 6^+ \to 4^+ \to 2^+ \to 0^+$ sequence, have been observed. Their energies and intensities are given in Table 1.1. In the article, the conclusion is made that the level population up to 8^+ is in agreement with a Gamow-Teller β decay of a 7^+ ground state in ^{182}Tl.

E_γ (keV)	I_γ rel.	Transition
351.4	100	$2^+ \to 0^+$
261.4	60	$4^+ \to 2^+$
333.3	30	$6^+ \to 4^+$
413.8	20	$8^+ \to 6^+$

Table 1.1: Energies and relative intensities of γ lines observed in ^{182}Tl β decay. The table is adopted from article [Bou91].

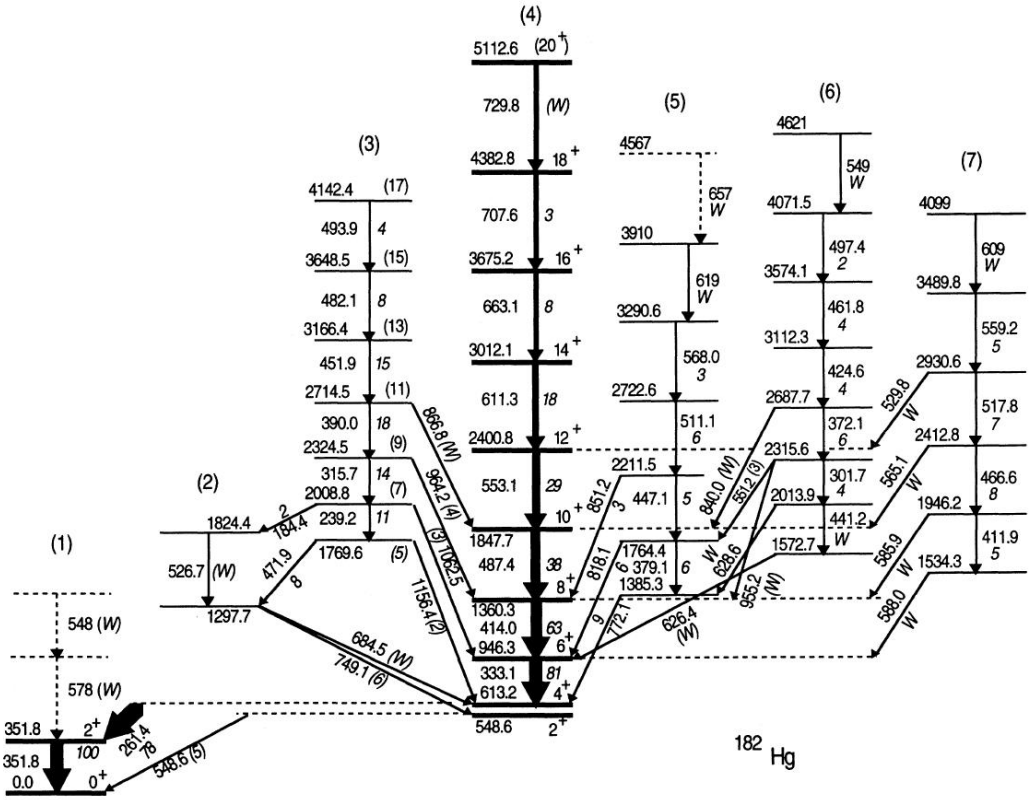

Figure 1.17: Excited level scheme of ^{182}Hg. Transitions indicated with *(W)* were only weakly observed. This figure was adapted from [Bin95].

Chapter 2

Experimental setup

Studies of ^{200}Fr and ^{182}Tl, were carried out at the ISOLDE facility [ISO10] at CERN (European Organization for Nuclear Research). The first section describes the ISOLDE facility and gives the information about the production rates of radioactive isotopes of interest. A description of the detection setup (chamber and detectors) is given in the other sections.

2.1 The ISOLDE facility

Beams of radioactive isotopes ^{200}Fr and ^{182}Tl were provided by the ISOLDE facility at CERN. The schematic layout of the facility is depicted in Fig 2.1.
The PSB (Proton Synchrotron Booster) at CERN accelerates protons using four small synchrotrons. A beam of protons with an energy of 1.4GeV and with an intensity of 3.2×10^{13} is produced in a pulse mode of 1.2 s. A sequence of 21 pulses is referred as a super cycle.

To produce the radioactive ion beam of ^{200}Fr or ^{182}Tl, the proton beam impinges ^{238}U nuclei. The protons induce spallation, fission and fragmentation of ^{238}U, creating an enormous amount of different isotopes. The products of these reactions diffuse out of the target.

2.1.1 Ionization source

The atoms of interest have to be ionized, so they can be accelerated to form a radioactive beam. Therefore they are diffusing to an ion source through a heated transfer line. There are three main ionization methods; surface ionization, ionization by electron impact and resonant laser ionization.
In the decay study of ^{200}Fr, surface ionization was used since Fr has a very low ionization potential (Fig 2.2). A transfer line of tantalum is heated up. Due to the high work function of Ta and the low ionization potential of Fr, The Fr nuclei leave the transfer line in a 1^+ charge state (Fig 2.3a).

Tl atoms have a ionization potential that is too high to have efficient surface ionization. Therefore resonant laser ionization was used to ionize the Tl atoms passing through the transfer line (Fig 2.3b). Lasers of different wavelength excite stepwise and eventually ionize a specific element by using different atomic transitions. The atomic transitions are element

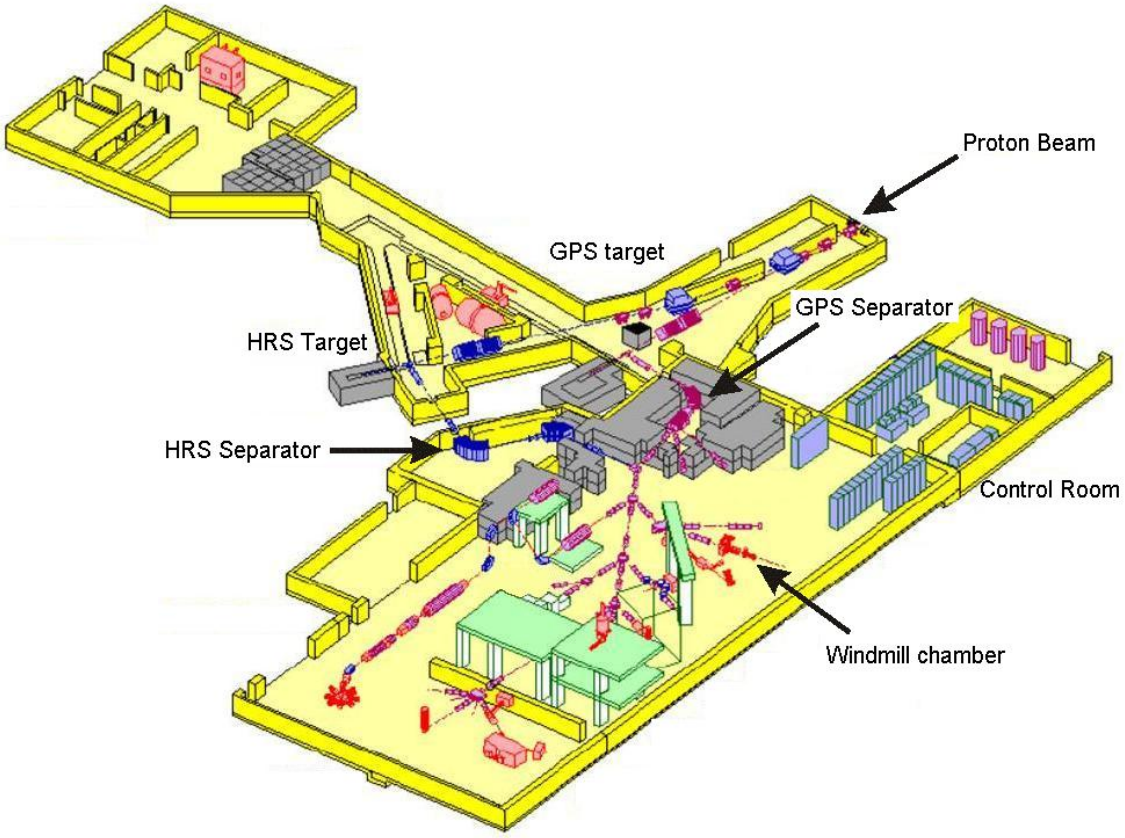

Figure 2.1: Layout of the ISOLDE facility at CERN [ISO10].

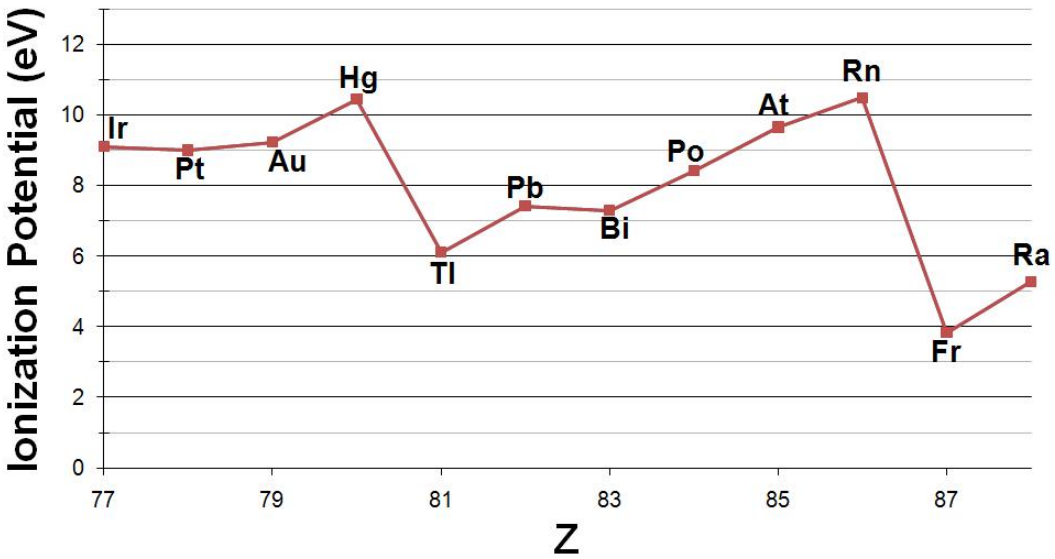

Figure 2.2: Overview of the ionization potentials of all elements with $77 \leq Z \leq 88$ [Moo70].

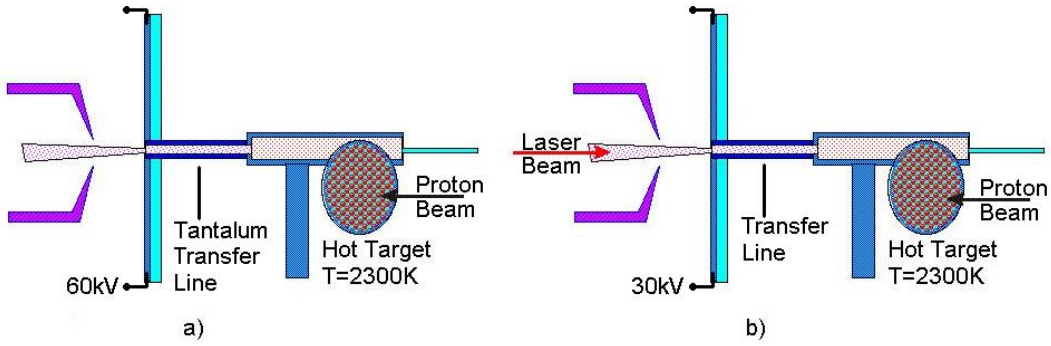

Figure 2.3: Schematic picture of a) the production of Fr isotopes with a surface ion source and b) the production of Tl isotopes with a laser ion source [ISO10].

specific (see Fig 2.4 for the case of Tl) so laser ionization is a highly element-selective ionization method.

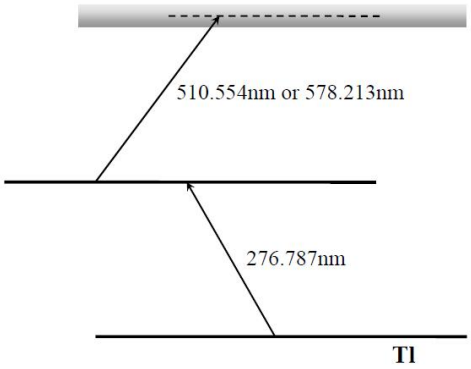

Figure 2.4: Atomic transition of Tl used for resonant laser ionization [Fed03].

After ionization the radioactive ions are extracted from the ion source by extraction electrodes. The radioactive isotopes are accelerated by a potential difference to the mass separator. At ISOLDE there are two mass separators, the General Purpose Separator (GPS) and the High Resolution Separator (HRS) [ISO10], which are used to select ions with a certain mass. The GPS consists out of one analyzing magnet and has a mass resolving power $m/\Delta m$ of 2400. The HRS is equipped with two analyzing magnets and has a higher mass resolving power $m/\Delta m$ of 5000.

Electrons are accelerated by the potential difference in a direction opposite to the beam direction. These accelerated electrons have a small probability to reach the target and ionize elements in the U target. All isobars pass through the analyzing magnet, since it is only mass selective. Therefore the ion beam is contaminated with different elements with the same mass. The mass selection is not perfect, but instead has some distribution that peaks around the preferred mass. Therefore, also ions with other masses can pass through the analyzing magnet and contaminate the ion beam.

2.1.2 Production rates

The alpha spectra used for the first part of this thesis on the decay of ^{200}Fr, were obtained in 2009 during experiment IS456. In run 190 and 240 of this experiment, the GPS was set to select isotopes with $A \approx 200$. During run 190, 6 proton pulses from every supercycle were used and data was collected for about an hour and a half. During run 240, 7 proton pulses were used and data was collected for 68 minutes. The yield for ^{200}Fr at ISOLDE with a UC_x target was 2×10^{-1} ions/s. After extraction out of the surface ion source, the radioactive isotopes were accelerated to 50 keV.

One run in experiment IS466 was dedicated to observe the decay of ^{182}Tl. Decay data were taken for 22 minutes using 2 proton pulses from the supercycle. The yield for ^{182}Tl at ISOLDE with a UC_x target equals 6.4×10^4 ions/s. After extraction out of the resonant laser ion source, the radioactive isotopes were accelerated to 30 keV and the HRS was used for mass separation.

The proton pulse impinges for 2.4 μs on the U target. The diffusion and ionization processes take some time, therefore the ion beam has a certain release time, which is dependent on the chemical element that is produced. The release time for Tl ions is given in Fig 2.5.

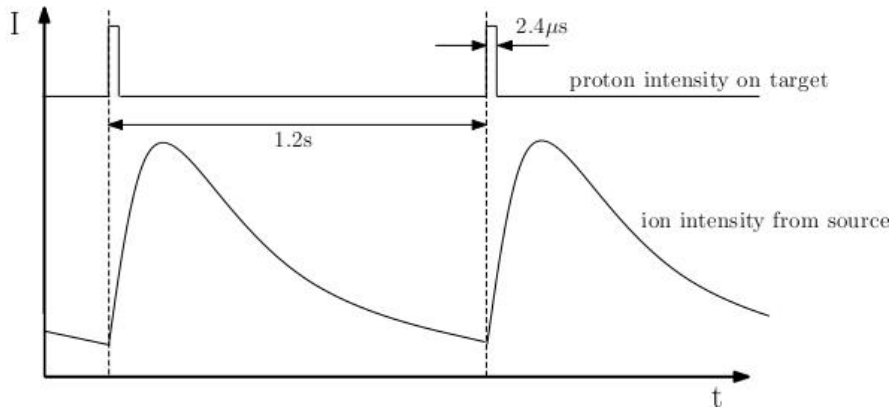

Figure 2.5: Schematic time structure of the proton and Tl ion beam. The picture was adpated from [Els09].

2.2 Windmill Chamber

The radioactive ion beam was implanted on thin carbon foils inside the windmill chamber (Fig 2.6), which was kept at vacuum. At the entrance of the chamber, a collimator in combination with a Faraday cup was used to optimize the beam current. For these experiments a collimator with a diameter of 5 mm was used.
The carbon foils had a thickness of ≈90 nm (=20 μg/cm^2) only, in order to minimize the energy loss of α particles and fission fragments going through the foil. The implantation depth for a 50 keV beam is 27 nm and for a 30 keV beam it is 18 nm. Ten such carbon foils were mounted on a rotating wheel inside the windmill chamber. The position in the chamber where the beam was entering, is referred to as the implantation station. The

wheel was rotated by a step motor, to bring away the activity and present a fresh foil at the implantation station. Long lived activity in the foils was detected at a second position in the chamber, called the decay station. By rotating the wheel over 144°, the foil at the implantation station was transported to the decay station. This was done after every supercycle.

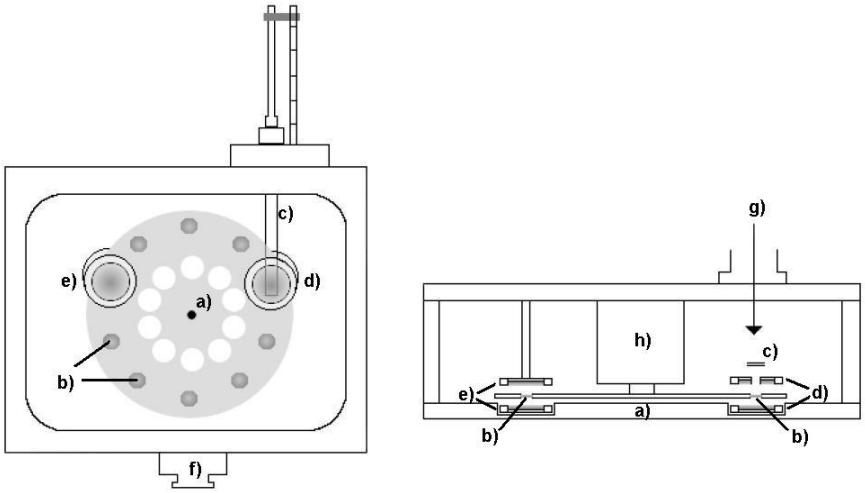

Figure 2.6: Windmill chamber, left: back view of the chamber; right: top view of the chamber. a) rotating wheel, b) carbon foils, c) current measurement and collimator, d) implantation station with two silicon detectors, e) decay station with two silicon detectors, f) pumping hole to obtain vacuum, g) separator beam, h) step motor [Coc10].

2.3 Silicon detectors

Four silicon detectors were mounted inside the chamber to detect fission fragments, α and β particles: two at the implantation station and two at the decay station. Positioning of the silicon detectors at both sides of the foils had two main advantages. The geometric efficiency was increased and both fission fragments, which are emitted back-to-back, could be recorded in coincidences.

Two Passivated Implanted Planar Silicon (PIPS) detectors (300 mm^2 active area) from Canberra [Can10] were used. One PIPS was positioned at the decay station, the other one at the back of the foil (with respect to the incoming beam) at the implantation station. The second silicon detector at the decay station was a Totally Depleted Silicon Surface Barrier (SSB) detector (300 mm^2 active area) from Ortec [Ort10]. In front of the foil, where the beam had to pass through, an Annular Partially Depleted Silicon Surface Barrier Detector from Ortec was used. It had a circular hole with a diameter of 6 mm in the middle of the detector so that the ion beam could pass through (Fig 2.7a). The annular detector had an active area of 450 mm^2. The resolutions of all detectors were between 15 and 20 keV.

The distance between the foil and the annular detector could not be too small because most of the α particles would fly through its hole. The distance could not be too large either because the solid angle for detection would be too small. The optimal distance for

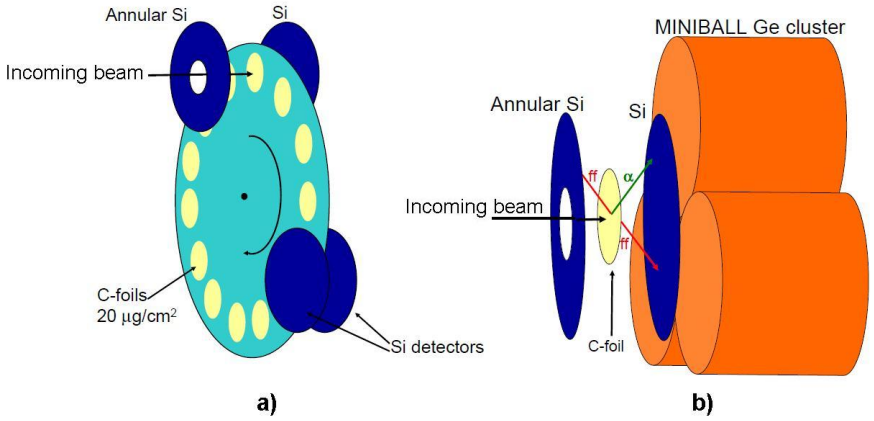

Figure 2.7: a) Position of the silicon detectors at the implantation station and decay station. b) Position of the germanium detectors outside the windmill chamber.

the annular detector is at 4 mm distance of the foil (Fig 2.8). For technical reasons, the annular detector in these experiments was positioned at 7 mm of the foil. At this distance, the annular detector covered a solid angle of 20 %.

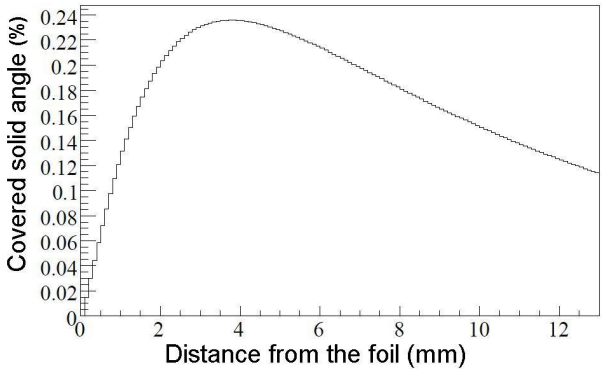

Figure 2.8: Solid angle covered by the annular detector as a function of the distance from the carbon foil. The solid angle peaks at a distance of 4 mm. [Coc10]

The Si detectors are made of a junction of a layer n-type and a layer p-type semiconductor materials [Kno99]. Because the n-type has an excess of conduction electrons with respect to the p-type, a migration of charge carriers takes place at the junction. This way a depletion region is formed with immobile positive charges at the n-type side and immobile negative charges at the p-type side of the crystal. The depletion region can be extended by applying a reverse-bias voltage. When an energetic particle passes through the depletion region, it deposits its energy by creating electron-hole pairs. The number of created electron-hole pairs is proportional to the energy of the incident particle. The electric field across the depletion region collects the electron-hole pairs. This gives an electric current also proportional to the energy of the incident particle.

The p-type and n-type materials for the PIPS detector were formed by implanting acceptor

(B) ions at on side of a high purity silicon wafer and donor (As) ions at the other side of the wafer. The SSB detector was formed by evaporating gold, a p-type material, on a n-type silicon crystal. Both types of Si detectors were characterized by a very thin dead layer, an important consideration for a good energy resolution.

2.4 Germanium detectors

Behind the implantation station, outside the windmill chamber, a Miniball cluster was placed to detect the γ radiation (Fig 2.7b). This Miniball cluster consisted out of three encapsulated six-fold segmented high-purity germanium crystals [MIN10]. Each of the three crystals was kept at high vacuum and was cooled down by a triple cluster cryostat with liquid nitrogen. The combination of Si detectors and Ge detectors at the implantation station, allowed to measure fission-γ and α-γ coincidences. The three Ge crystals of the cluster detector could be read out separately, allowing to look for γ-γ coincidences.

The high-purity Ge was made by locally heating a Ge sample and slowly passing a melted zone from one end of the sample to the other end. The impurities are more soluble in the melted zone, so they were swept away out of the sample with the melted zone. By repetition of this process, impurity levels as low as 10^9 atoms/cm^3 could be achieved. Crystals of n-type Ge were grown from this high-purity Ge and a p-type contact was produced by implanting B atoms. The detecting method was the same as for the Si detectors discussed above. Electron-hole pairs were created by particles passing through the depleted region and a current proportional to the energy of the incident particle was created.

The three Ge crystals were encapsulated separately to help preserve the properties of the detectors over many years [Ebe01]. This enhanced the reliability of the Miniball cluster detector considerably.

Chapter 3

Data analysis of the α decay of ^{200}Fr

Recently, the β delayed fission of ^{196}At was discovered at SHIP in Darmstadt [And]. As mentioned before, it is important to know the EC/β^+ branching ratio of ^{196}At to investigate the fission probability. In this chapter, the data analysis, which was performed to determine the branching ratios of ^{196}At, is discussed. This is done by looking at the decay chain of ^{200}Fr. First, α spectra obtained in experiment IS456 in the year 2009 at ISOLDE are handled. Further, branching ratios for ^{196}At are calculated. Finally, the results are compared with the previously obtained result [Wit05].

3.1 Measured nuclei

To determine the α- and EC/β^+-branching ratios, a number of runs of experiment IS456 were used. A summary of the details of all these runs can be found in Table 3.1.

Run	Lasers to Po	A	Δt (m)	Proton pulses
190	Off	200	90	2,4,11,12,13,15 (of 15)
239	Off	211	120	No
240	Off	200	68	3,6,9,12,14,15,18 (of 18)
224-227	On	216	170	No
230-233	On	218	360	No

Table 3.1: Summary of the details of the runs of experiment IS456, used in the present thesis. It is indicated whether the proton pulses and the lasers were used. Further it is indicated which mass A the GPS separated and how long the data was collected.

3.1.1 Run 190 and 240

In experiment IS456 at ISOLDE, runs 190 and 240 were dedicated to study ^{200}Fr. Fr atoms have a low ionization potential, see Fig 2.2, therefore they were ionized by the hot walls of the U target. ^{200}At and ^{200}Po have relative high production yields (1.6×10^6 ions/s and 1.6×10^7 ions/s), with respect to ^{200}Fr (2×10^{-1} ions/s) [ISO10]. ^{200}At and ^{200}Po atoms

were ionized by accelerated electrons and they contaminated the beam. In the α spectra from both runs, which are represented in Fig 3.1, decays of ^{200}Fr, ^{200}At and ^{200}Po were observed. The α branching of ^{200}Fr is 100% [Fir99]. The α decay of daughter nucleus ^{196}At was also detected. Other daughter nuclei were not observed.

In run 239, no proton pulses were used. Only the long lived $^{224-229}$Ac, $^{223-228}$Ra and $^{221-224}$Rn were still present in the hot target. By several α and β^- decay of these long lived nuclei, $^{220-224}$Fr were produced, which were surface ionized. Two hours later run 240 was performed. The half-lives of $^{220-224}$Fr range from 27.4 s to 21.8 min, therefore almost all Fr had decayed before run 240. Longer lived daughter nuclei ^{212,213}Bi and ^{211,212}Pb were still present during run 240 and contaminated the α spectrum. The α peaks of ^{211,212}Bi and ^{212,213}Po are visible in the spectrum of run 240, see bottom spectrum of Fig 3.1.

Fr atoms have high production yields at the U target and have a high ionization probability. Due to collisions in the beam line and the moderate mass resolving power of the GPS, Fr nuclei with $A > 200$ were contaminating the beam line. Therefore the peaks between 6600 keV and 7000 keV were tentatively attributed to $^{205-209}$Fr as depicted in Fig 3.1.

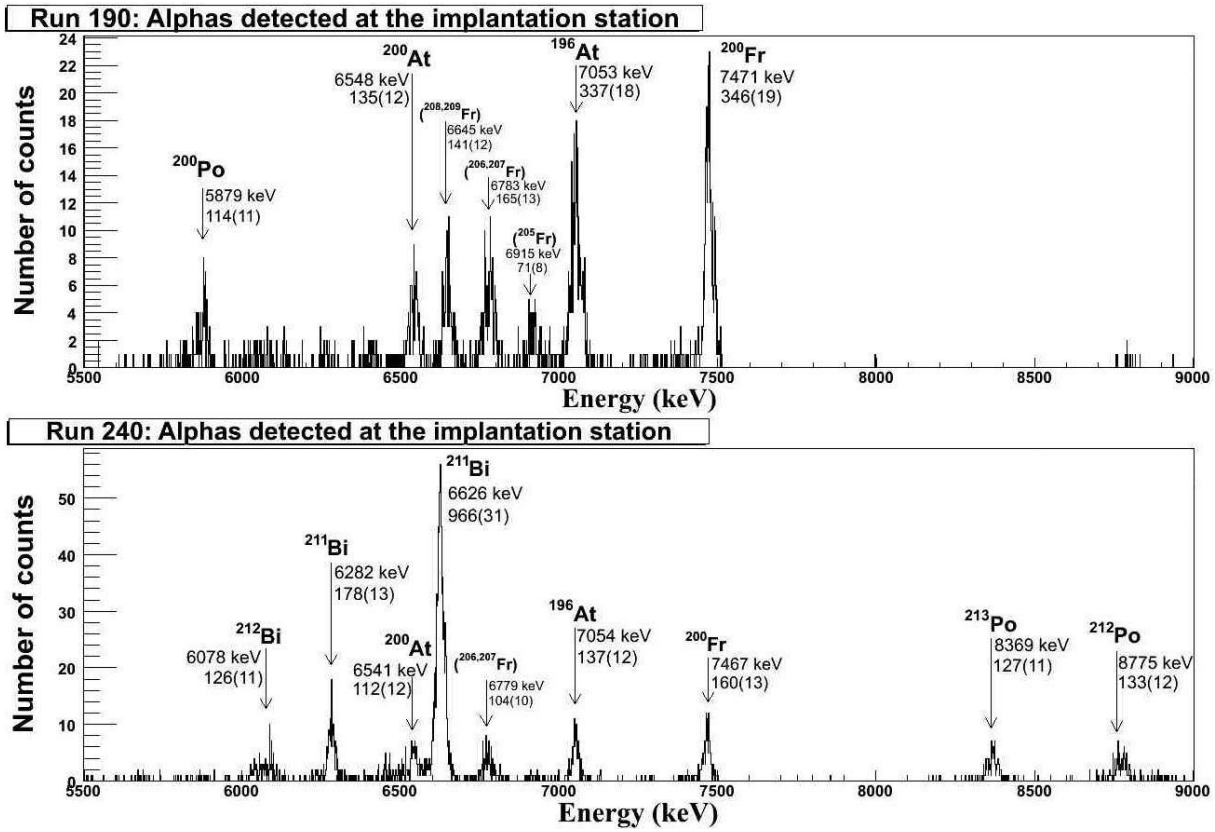

Figure 3.1: α spectra of run 190 (top spectrum) and run 240 (bottom spectrum). Energies and number of counts for each peak are indicated.

The α spectra of run 190 and 240 are given in Fig 3.1. There is not enough data collected to fit the peaks with a Gaussian function, therefore the integrals were taken as intensities of the peaks. The error bar on the intensity is the square root of the integral value.

Figure 3.2: Representation of the decay processes in runs 190 and 240. Nuclei which were implanted during these runs are indicated in red. Contaminating nuclei with long half-lives from run 189 are denoted in purple, from run 239 in green.

A summary of all implanted and contaminating nuclei is given in Fig 3.2. Although in both experiments there are some contaminating nuclei, α peaks of ^{200}Fr and ^{196}At are well resolved, see Fig 3.1. Some peaks have large tails, depending on how much energy the α particle looses by going through the carbon foil.

3.1.2 Run 224-227 and 230-233

Runs 224-227 were dedicated to study ^{216}Po. Laser ionization (see section 2.1) was used to ionize Po isotopes, while the GPS separated isotopes with mass $A \approx 216$. Runs 230-233 were realized to investigate ^{218}Po. Laser ionization was used to ionize Po isotopes, the GPS separated isotopes with mass $A \approx 218$. Corresponding α spectra for the back and annular detector are given in Fig 3.3. In these runs, ^{221}Fr was contaminating the radioactive beam. The α spectra in Fig 3.3 shows that the α decay of ^{221}Fr and the subsequent α decay of ^{217}At were observed in these runs.

3.2 Recoil losses

A mean implantation depth in carbon of 23.9 nm was calculated by SRIM [SRI08], for 50 keV ^{200}Fr ions. This is about a third of the thickness of the carbon foil. The Q value of the α decay of ^{200}Fr is 7621.5 keV [Fir99]. Solving equations 1.10 and 1.11 shows that ^{196}At has a recoiling energy of 152.4 keV. The stopping range of ^{196}At ions with an energy of 152 keV was calculated to be 47.9 nm by SRIM, which is twice as large as the implantation depth of ^{200}Fr.

Therefore, a significant amount of ^{196}At ions, recoiled out of the foil, in direction of the annular detector. In contrast, a negligible amount escaped the foil at the side of the back detector. When the recoiling ^{196}At is implanted in the annular Si detector, the probability to detect the subsequent α decay is much higher for the annular detector than for the back

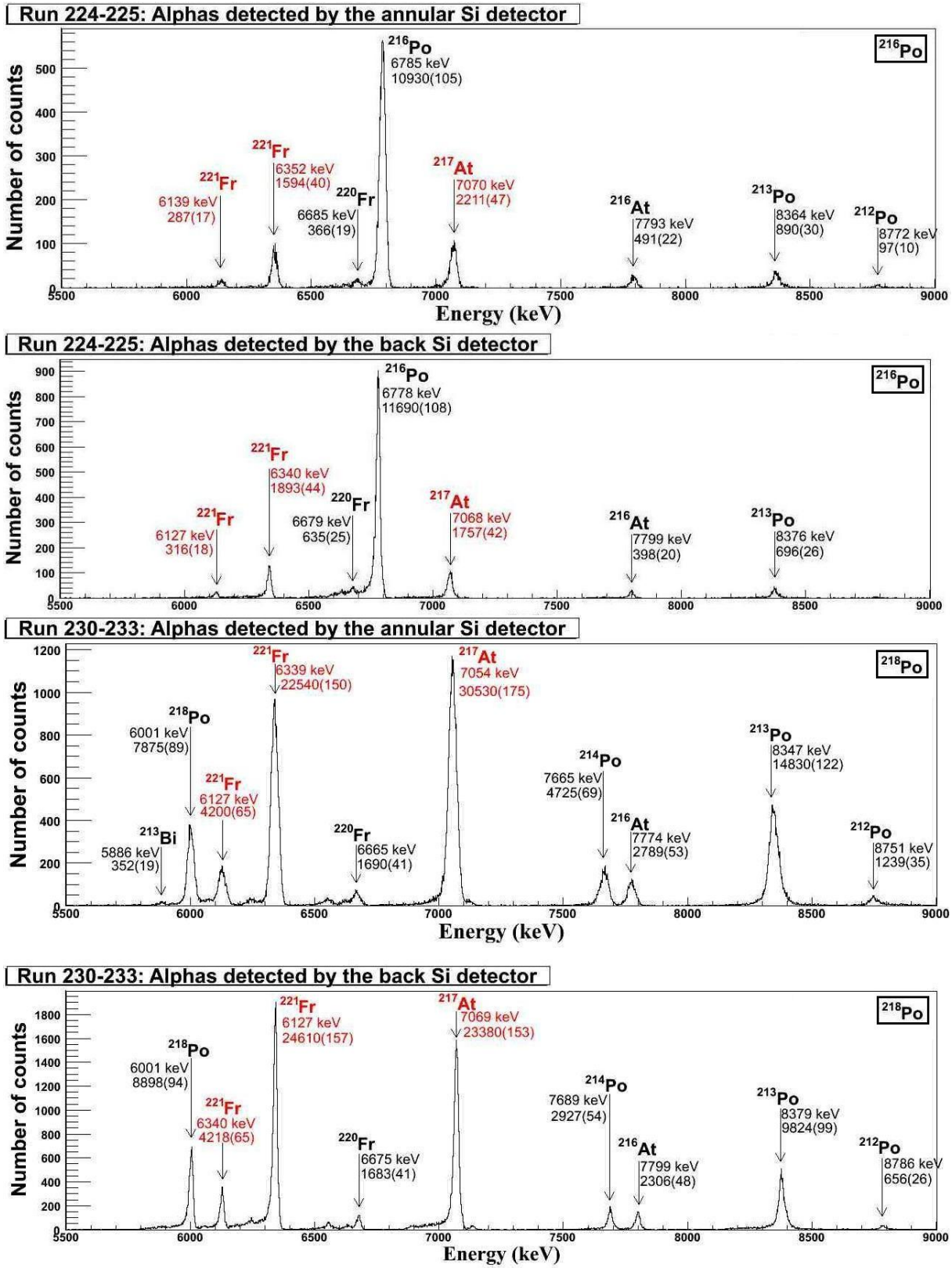

Figure 3.3: Runs 224-227 (top two spectra): α spectra obtained by the annular (first spectrum) and the back (second spectrum) Si detector at the implantation station. Runs 230-233 (bottom two spectra): α spectra obtained by the annular (third spectrum) and the back (fourth spectrum) Si detector at the implantation station.Energies and intensities for each peak are indicated. The peaks used to determine the correction factors are indicated by red.

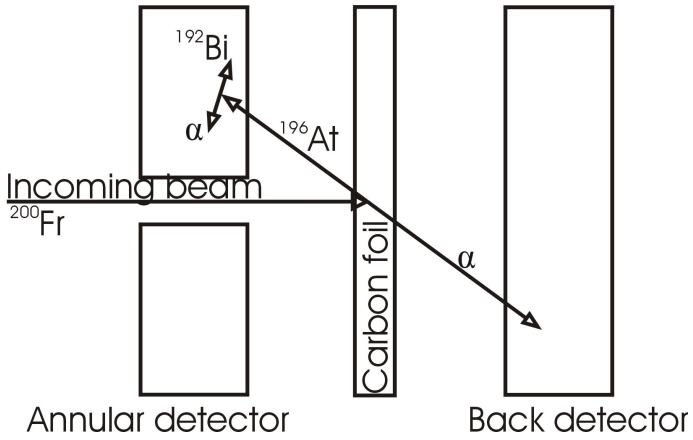

Figure 3.4: The recoiling ^{196}At nucleus could be implanted into the annular Si detector with certain probability. Subsequent α decay of ^{196}At has a high probability to be detected in the annular Si detector.

detector, see Fig 3.4. This explains different ratios $N(^{196}\text{At})/N(^{200}\text{Fr})$ between the back and annular detector, see Fig 3.5.

To find correction factors for this recoiling effect, runs 224-227 and 230-233 were used, where the α decay of ^{221}Fr and ^{217}At was observed. ^{221}Fr, $T_{1/2}$=4.9(2) m, decays 100% through α emission. Daughter nucleus ^{217}At, $T_{1/2}$=32.3(4) ms, has an EC/β^+-branching ratio of 0.012%, which is negligibly small [Fir99]. ^{217}At only occurs in the experiment as the daughter nucleus of ^{221}Fr, just as ^{196}At only originates from ^{200}Fr. The stopping range of ^{221}Fr in C is 24.8 nm [SRI08]. The Q value for the ^{221}Fr$\rightarrow^{217}$At is 6457.6 keV [Nat10], therefore, according to equations 1.10 and 1.11, the recoiling ^{217}At has an energy of 117 keV. The stopping range of ^{217}At is 41.6 nm.

	E (keV)	S (nm)		E (keV)	S (nm)
^{221}Fr	50	24.8	^{217}At	117	41.6
^{200}Fr	50	23.9	^{196}At	152	47.9

Table 3.2: Comparison of the implantation depth and recoil stopping ranges of ^{221}Fr$\rightarrow^{217}$At and ^{200}Fr$\rightarrow^{196}$At [SRI08].

Since the stopping ranges of ^{221}Fr and ^{217}At are comparable with the stopping ranges of ^{200}Fr and ^{196}At, the ratio of the number of counts of the α decays of ^{221}Fr and ^{217}At, can be used as correction factors for the recoiling of ^{196}At.

For ^{221}Fr, α lines with energies $E_\alpha = 6127$ keV and $E_\alpha = 6339$ keV give 98.5 % of the total α intensity of ^{221}Fr, denoted by N_{Fr} [Fir99]. The α line with energy $E_\alpha = 7054$ keV, gives 99.9 % of the total α intensity of ^{217}At, denoted by N_{At} [Fir99]. For runs 224-227, the total number of counts of detected α's in the back and annular detector and the obtained correction factors are summarized in table 3.3.

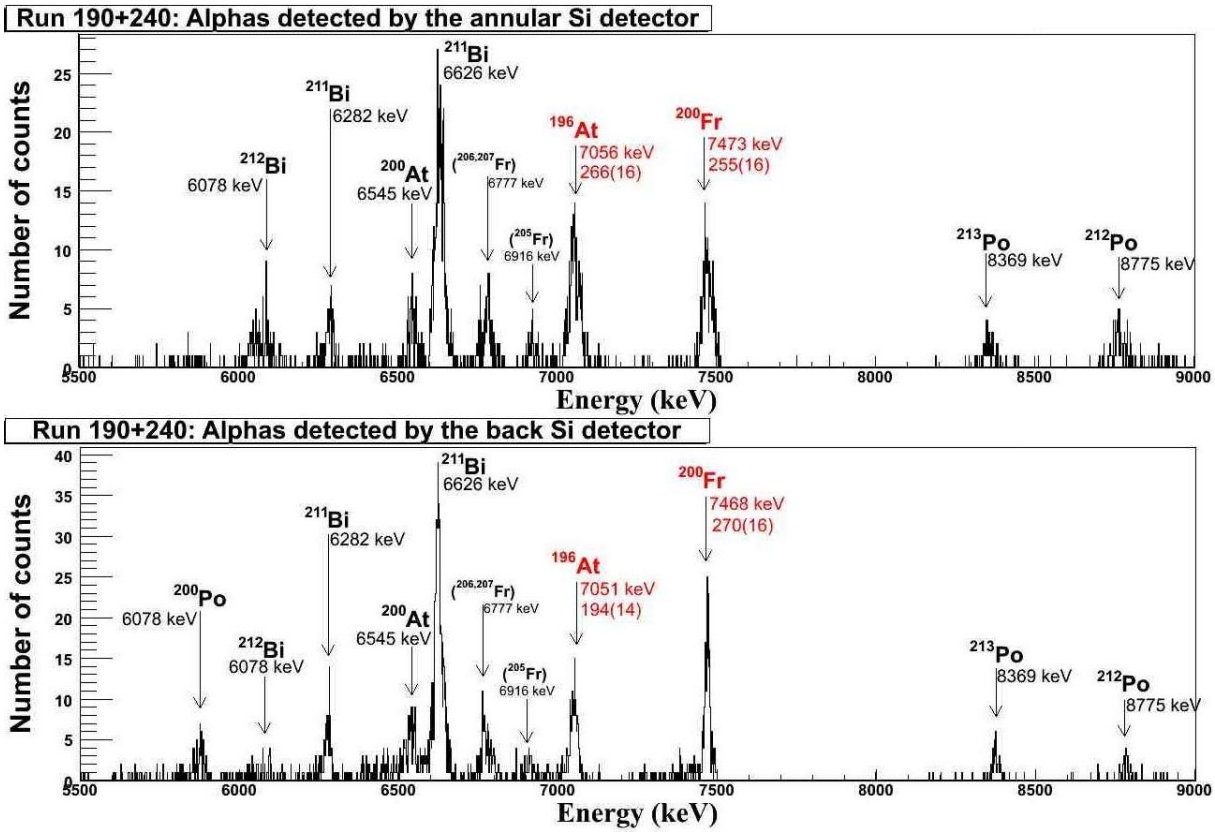

Figure 3.5: Runs 190 and 240: α spectra obtained by the annular (top spectrum) and the back (bottom spectrum) Si detector at the implantation station. All peaks are identified and their energies are given. The intensity of the α peak is only indicated for nuclei which are discussed in this section (red). When the identification is not fully certain, the name is put between brackets.

Runs	^{221}Fr			^{217}At		Corr. factors
224-227	N(6127 keV)	N(6339 keV)	N_{Fr}	N(7054 keV)	N_{At}	N_{Fr}/N_{At}
Annular	287(17)	1594(40)	1910(44)	2211(47)	2213(47)	**0.863(27)**
Back	316(18)	1893(44)	2243(48)	1757(42)	1759(42)	**1.275(41)**

Table 3.3: The number of counts per peak in the annular and back detector during runs 224-227 are summarized. The total number of α's detected at the back and annular detector are calculated using the α intensity corrections given in the text. The ratios N_{Fr}/N_{At} give the correction factors for the annular and the back detector.

Applying the same method to the data from runs 230-233 gave the correction factors in table 3.4.

Runs	^{221}Fr			^{217}At		Corr. factors
230-233	N(6127 keV)	N(6339 keV)	N_{Fr}	N(7054 keV)	N_{At}	N_{Fr}/N_{At}
Annular	4200(65)	22540(150)	27147(166)	30530(175)	30561(175)	**0.888(7)**
Back	4218(65)	24610(157)	29267(225)	23380(153)	23403(153)	**1.251(13)**

Table 3.4: The number of counts per peak in the annular and back detector during runs 230-233 are summarized. The total number of α's detected at the back and annular detector are calculated using the α intensity corrections given in the text. The ratios N_{Fr}/N_{At} give the correction factors for the annular and the back detector.

Within experimental uncertainties, both used data sets, i.e. runs 224-227 and runs 230-233, gave the same value of correction factors. Averaging these two values rendered final recoil efficiency correction factors of 0.876(7) for the annular detector and 1.263(12) for the back detector.

3.3 α- and EC/β^+-branching ratios of ^{196}At

The half-lives of ^{200}Fr and ^{196}At are 49 ms and 0.388 s respectively [Fir99]. All ^{200}Fr and ^{196}At nuclei had decayed during one supercycle, before the wheel was turned, thus no intensity correction for the refreshing of the foil had to be taken into account. The efficiency of the detector is almost constant for energies ranging from 5 to 10 MeV. Only a correction for the recoil effect needs to be considered. This correction can be made by using the correction factors obtained in the previous section.

The α branching ratio b_α of ^{196}At is interpreted as the intensity of its α peak in comparison with the intensity of the α peak of ^{200}Fr. The EC/β^+ branching ratio b_β is simply 1 minus the α branching ratio. The correction factors for the annular and back detector, were applied to intensities for the α decay of ^{196}At in table 3.5. According to the values of the annular detector, b_α = 91(8) %, using the values of the back detector b_α = 91(9)%. The two values are in very good agreement. Averaging the two values rendered the final value for the α branching ratio of ^{196}At: 91(6) %. The EC/β^+-branching ratio is equal to 9(6) %.

Runs		Before correction	After correction	
190,240	$N(^{200}$Fr)	$N(^{196}$At)		α branching (%)
Annular	255(16)	266(16)	233(14)	91(8)
Back	270(16)	194(14)	245(18)	91(9)

Table 3.5: The number of counts of 200Fr and 196At in the annular and back detector. Correction factors 0.876(7) and 1.263(12) were used for the annular and back detector respectively. The α branching is calculated by $N(^{196}\text{At})/N(^{200}\text{Fr})$

3.4 Comparison with previous values

Previously, $b_\alpha = 94(5)\,\%$ for ^{196}At was reported [Wit05]. In that experiment, only the back detector was present and a correction factor of 0.75% was used for this detector. Averaging their value with the value which was obtained in the present thesis, **a new value $b_\alpha = 93(4)\,\%$ was determined for ^{196}At and therefore $b_{\mathbf{EC}/\beta^+} = 7(4)\%$.**

Chapter 4

Data analysis of the β decay of ^{182}Tl

In this chapter, the data of experiment IS466 is presented and discussed. First, the single γ-rays spectrum which was obtained by the Miniball Ge cluster detector is shown and γ rays, which are associated with the decay of ^{182}Tl, are identified. Using these γ rays, a new value of $T_{1/2}$ of ^{182}Tl was determined. Further on, the coincidence spectra of the main γ peaks of ^{182}Tl decay were examined carefully and results were compared with GEANT4 Monte Carlo simulations. An $E0$ component in the transition between coexisting 2^+ states, was identified. Finally, the level scheme of ^{182}Hg (daughter nucleus of ^{182}Tl) which includes all γ rays observed in the present work, has been constructed.

4.1 Single γ-rays spectrum

The β decay of ^{182}Tl feeds nuclear excited states of ^{182}Hg. When the energy of the excited state is higher than or comparable to the height of the fission barrier, delayed fission and electromagnetic processes compete, see Section 1.2.4. Dominantly, the β decay populates the states of ^{182}Hg with low excitation energy (<1 MeV). These states deexcite through electromagnetic processes, such as γ-ray emission and internal conversion.

Figure 4.1 gives the spectrum of all γ rays detected at the Miniball Ge cluster. The half-life determination, see following section, has been used for the identification of peaks which are associated with the ^{182}Tl decay. The energies of other γ peaks were compared with the available data in the *Table of Isotopes* [Fir99] and the *National Nuclear Data Center* [Nat10] and their origins are indicated in Fig 4.1.

The γ rays depopulating the 2^+, 4^+, 6^+ and 8^+ states, which were identified in the in-beam experiment [Bin95], are clearly seen in the γ spectrum in Fig 4.1 at energies 351 keV, 261 keV, 332 keV and 413 keV. The KX rays arise from atomic relaxation after internal conversion and electron capture decay. The energy resolution of the Miniball detector for all γ peaks were between 2 and 4 keV. Taken the statistical error, and the calibration error into account, the error on the energy was estimated to be 0.5 keV.

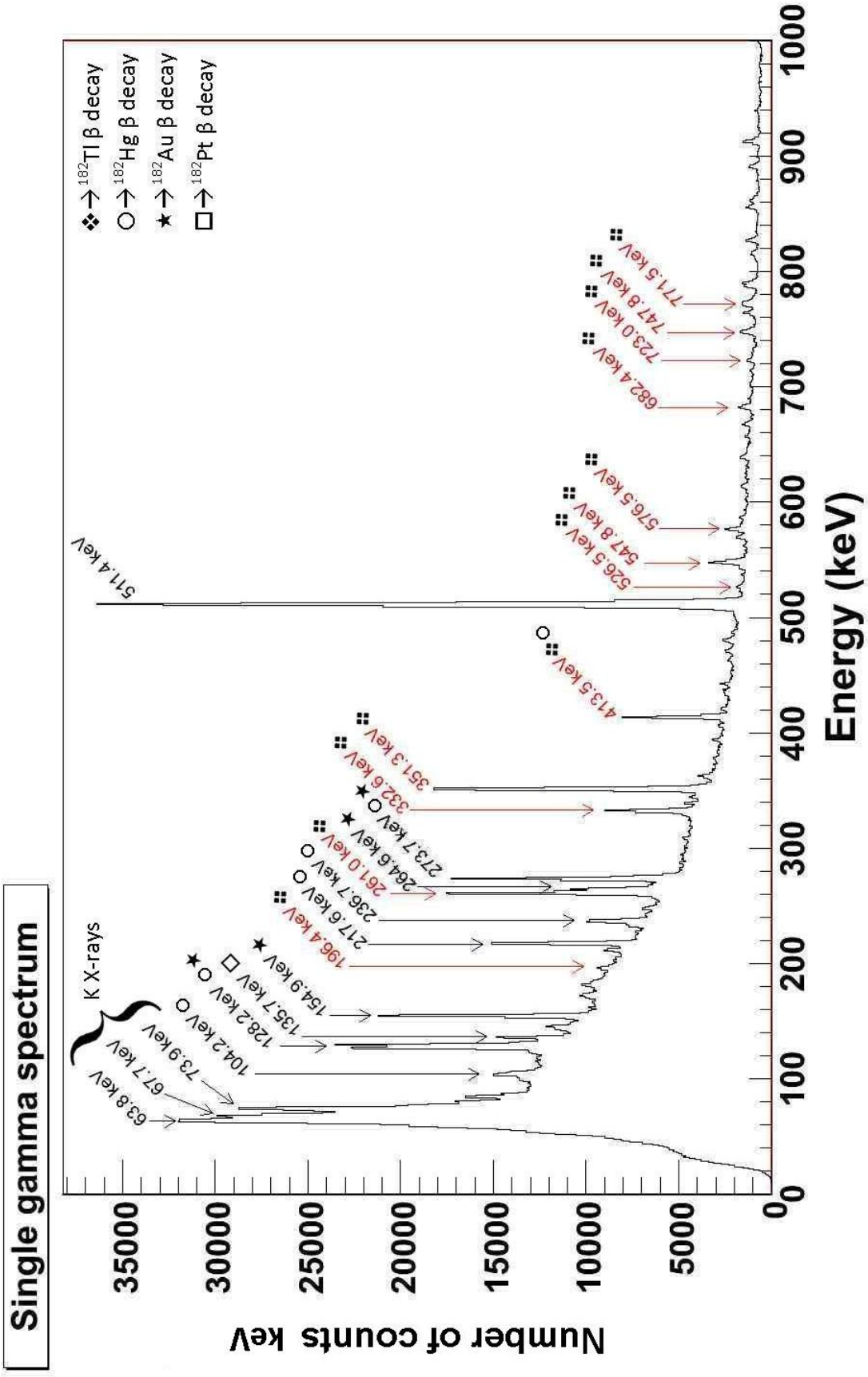

Figure 4.1: Single γ spectrum from experiment IS466, detected by the Miniball Ge cluster detector.

The relative peak efficiency ε was determined using a ^{152}Eu source and proven by the GEANT4 model of the windmill chamber [Ven10]. It is given by the following formula:

$$\varepsilon = 353.05658 \times E_{\gamma}^{-0.68895} \ , \tag{4.1}$$

where E_γ is the γ-ray energy in keV.

At the end of this chapter, the relative transition intensities, corrected for the peak efficiency of the Ge detector, are summarized in Table 4.2.

4.2 Determination of the half-life of ^{182}Tl

As the time difference between the beginning of the supercycle and the detection of the γ ray is recorded, time spectra can be created for γ rays with a particular energy and its background left and right. The background time spectra were normalized to the peak-to-background ratio and subtracted of the time spectrum of the investigated peak. This method was applied to the strongest γ peaks of ^{182}Tl, ^{182}Hg and ^{182}Au decay, with energies 351.3 keV, 217.6 keV and 154.9 keV respectively. The resulting time spectra are shown in Fig 4.2(a).

The decays of these three nuclei clearly have different time characteristics. The intensity of ^{182}Tl decay has a very steep rising between 1.2 s and 3.6 s. The second an third proton pulse from every supercycle were used only. The steep rising corresponds with the time that the ion beam was being implanted in the carbon foil, see Section 2.1.2. Once the implantation time is over, the activity of ^{182}Tl follows an exponential decay curve.

The daughter nucleus ^{182}Hg, $T_{1/2}$ =10.83(6) s [Nat10], was only produced via β decay of ^{182}Tl. Therefore it has a slower growing of its activity as shown in the time spectrum in Fig 4.2(a). The activity of the subsequent daughter nucleus ^{182}Au, $T_{1/2}$ =15.6(4) s [Nat10], has an even slower growing curve.

The $2^+ \rightarrow 0^+$, $4^+ \rightarrow 2^+$ and $6^+ \rightarrow 4^+$ are the strongest γ lines of ^{182}Tl decay. The $4^+ \rightarrow 2^+$ is close to another γ line, associated with the ^{182}Au decay [Fir99], thus the time decay curve contains the ^{182}Au decay part. Therefore, to determine the half life of ^{182}Tl, the sum of the time spectra of the $2^+ \rightarrow 0^+$ and $6^+ \rightarrow 4^+$ transitions was taken and the background was subtracted, see Fig 4.2(b). The decay curve was fitted with the exponential function:

$$I = p_0 e^{p_1 t} + p_2 \ . \tag{4.2}$$

The half life of ^{182}Tl is given by -$ln2/p_1$. The least-squares fit gives p_1=-0.2232 s^{-1}, therefore the half life of ^{182}Tl is 3.1(4) s.

The previously reported value was $T_{1/2}$ = 2.9(5) s [Ach09]. Averaging with the value obtained in this thesis, the new value of $T_{1/2}$ of ^{182}Tl is 3.0(3) s.

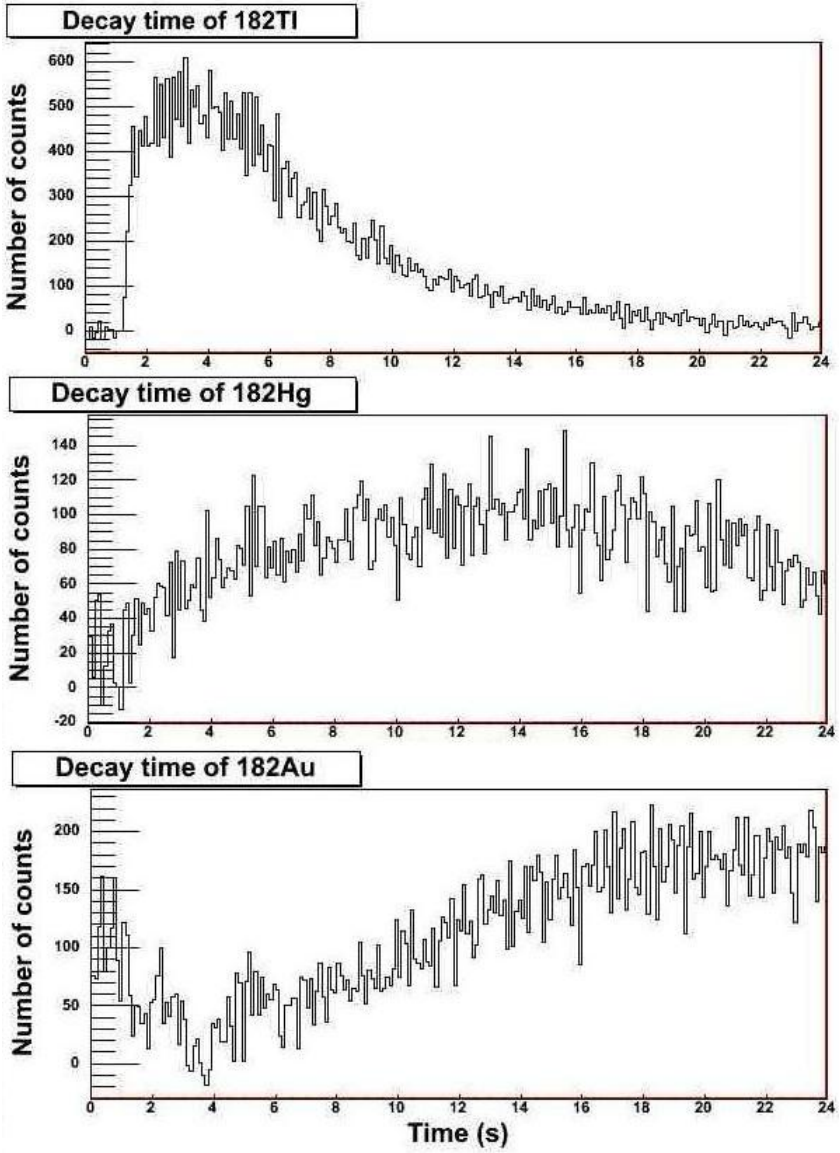

(a) Decay time spectra for ^{182}Tl, ^{182}Hg and ^{182}Au. The time spectra were produced by energy gates 351.3±2 keV, 217.6±2 keV and 154.9±2 keV respectively and subtracting the time spectra of nearby left and right background.

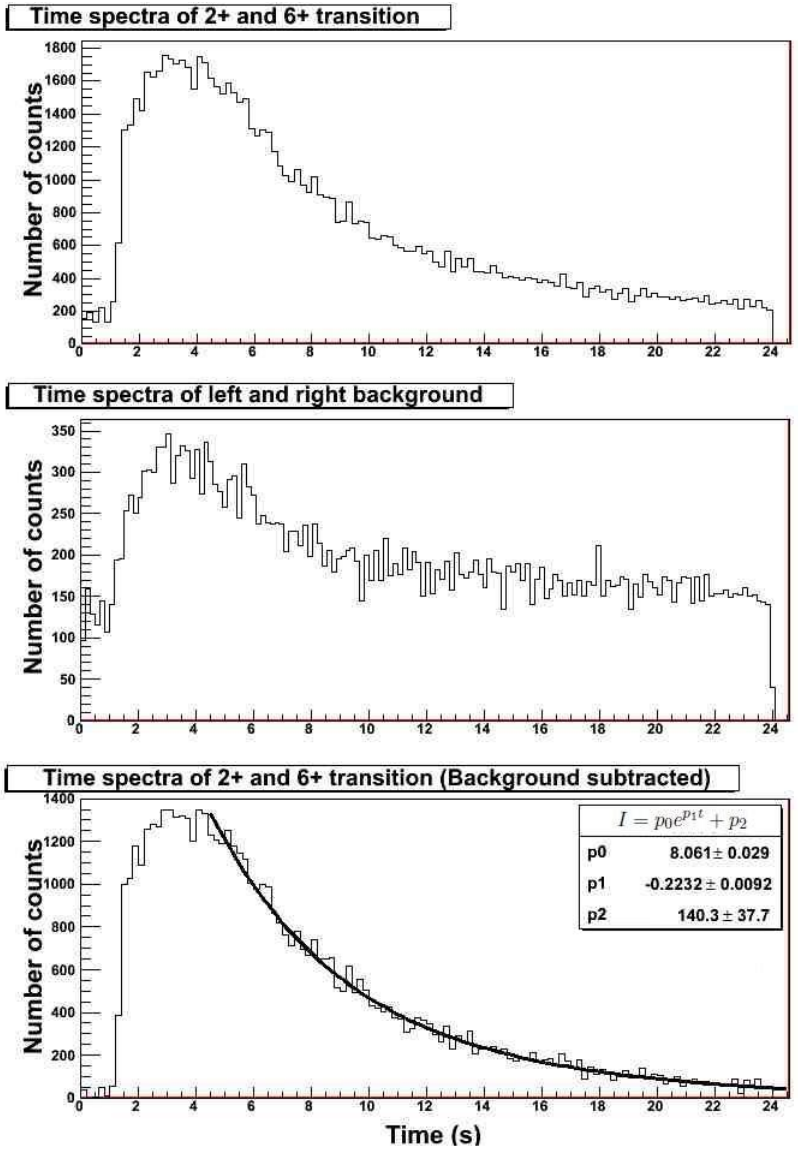

(b) The decay spectrum of ^{182}Tl, generated by gates on the $2^+ \rightarrow 0^+$ and $6^+ \rightarrow 4^+$ transitions (top spectrum), with the background spectrum (middle spectrum), with energy gates on 320-324 keV and 370-374 keV, subtracted (bottom spectrum).

Figure 4.2: Time spectra

4.3 $\gamma\gamma$ coincidences

An excited nucleus does not always decays directly to the ground state. Several subsequent γ rays can be emitted in cascade, feeding intermediate state(s). The typical half life of a nuclear excited state is in the order of tens of picoseconds. States with longer half lives are called isomers. If a γ ray is detected in one of the Ge crystals of the Miniball detector, coincident γ rays emitted by the same nucleus can be detected in one of the remaining crystals with a certain probability. Note, that an artificial pile-up peak can occur when more than one quanta interacted with the same crystal.

For a more detailed analysis, the data was sorted into a $\gamma\gamma$-matrix, with a condition on the time difference between both coincident γ rays $\Delta t(\gamma\gamma)$<200 ns. The $\gamma\gamma$ coincidences were investigated by projection of this matrix, using specific energy gates. The background, taken as the coincidence spectra on the left- and right-hand side of the peak in the energy spectrum, was normalized to the peak-to-background ratio and subtracted.

A specific problem, related to the Miniball segmented detector, was the strong sensitivity of the Compton scattering between the crystals. It can occur, that a γ ray deposits part of its energy in one crystal and the rest in another one. As a consequence of this, artificial peaks appear in coincidence spectra. For example, see Fig 4.3, where a 160 keV line is present in coincidence with the 351 keV transition. Since 351 and 160 sum up to 511, 160 keV is not a real transition, but only an artefact produced by projection of the $\gamma\gamma$ matrix. Note that 511 keV quanta are abundantly present. Also in the coincidence spectra of the $4^+ \rightarrow 2^+$, $6^+ \rightarrow 4^+$ and $8^+ \rightarrow 6^+$ transitions, artificial peaks with energies 250, 179 and 98 keV respectively, appeared (Fig 4.3). To the left and right of each artificial peak, a negative bump also appears, due to the right and left coincidence spectra, subtracted as background. Therefore these negative bumps are a signature of the artificial peaks.

The $2^+ \rightarrow 0^+$, $4^+ \rightarrow 2^+$ and $6^+ \rightarrow 4^+$ transitions in ^{182}Hg are clearly in coincidence with each other. This is in agreement with the level scheme which was obtained in the in-beam experiment [Bin95]. In the 8^+ coincidence spectrum, the $2^+ \rightarrow 0^+$, $4^+ \rightarrow 2^+$ and $6^+ \rightarrow 4^+$ transitions are observed. Thus the 8^+ state in ^{182}Hg is fed by β decay of ^{182}Tl. But inspection of the $8^+ \rightarrow 6^+$ coincidence spectrum, shows that a 128 keV line is present which cannot be seen in the subsequent $6^+ \rightarrow 4^+$, $4^+ \rightarrow 2^+$ and $2^+ \rightarrow 0^+$ cascade. This points to a doublet structure in the 413 keV line. Indeed, an experiment in 1974 [Cai74], reported γ peaks of 129 keV and 413 keV in the ^{182}Hg$\rightarrow^{182}$Au decay. Therefore, γ rays of 413 keV originate both from ^{182}Tl decay and ^{182}Hg decay and the 413 keV peak is a doublet.

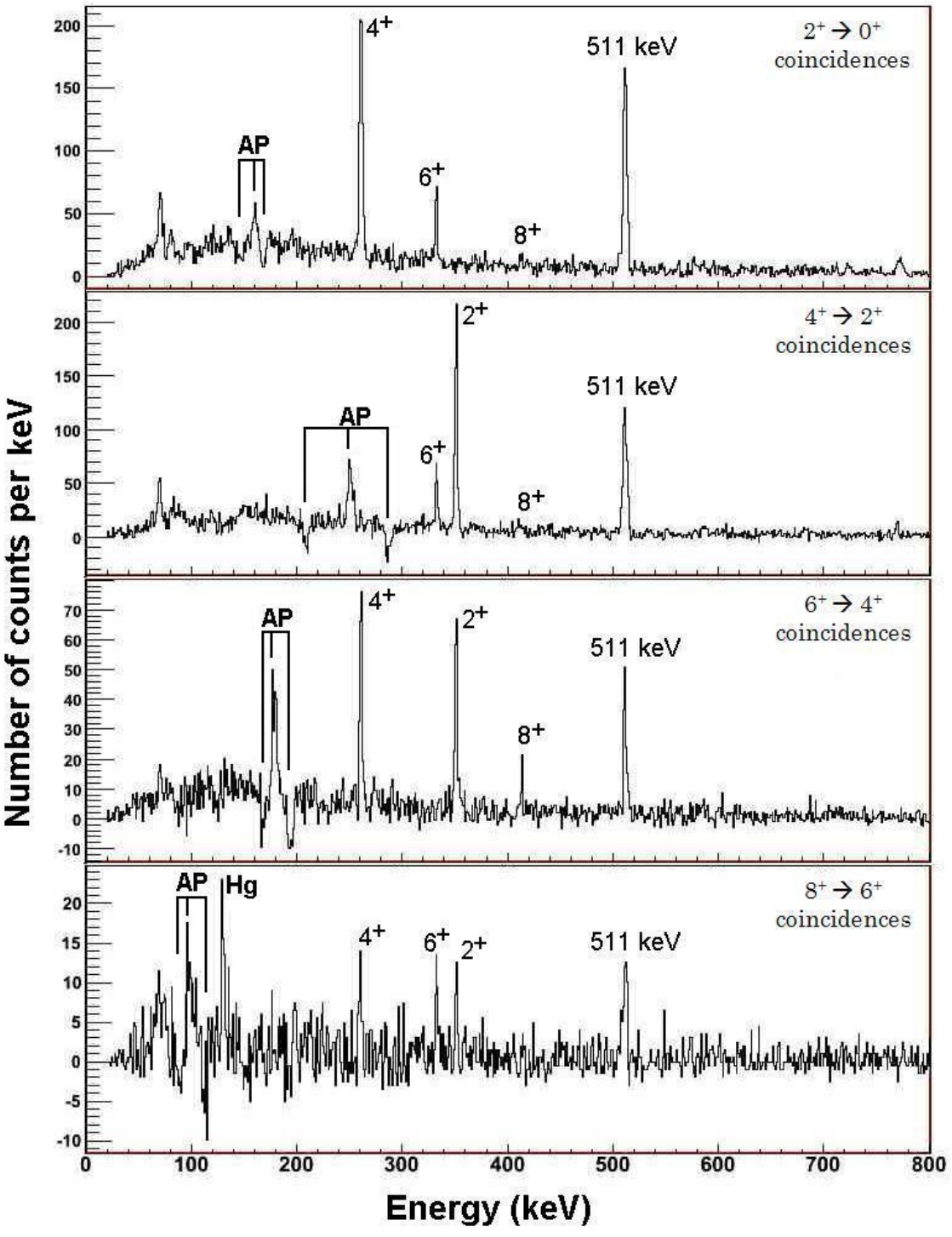

Figure 4.3: The coincidence spectra of the $2^+ \rightarrow 0^+$, $4^+ \rightarrow 2^+$,$6^+ \rightarrow 4^+$ and $8^+ \rightarrow 6^+$ transitions, with energies 351, 261, 332 and 413 keV respectively. The background was subtracted as mentioned in the text. AP stands for Artificial Peak.

4.4 Intensity of the $8^+ \rightarrow 6^+$ transition

Since the 413 keV γ peak is a doublet, the relative intensity of the $8^+ \rightarrow 6^+$ transition can not be determined by using the single γ spectrum. To determine the relative intensity of the $8^+ \rightarrow 6^+$ transition, GEANT4 Monte Carlo simulations were performed by M. Venhart. The simulated data were analyzed in the present thesis.

As an input for the GEANT4 simulation, the relative intensities of the $2^+ \rightarrow 0^+$, $4^+ \rightarrow 2^+$ and $6^+ \rightarrow 4^+$ transitions from the single γ spectrum were taken (corrected for the efficiency, see Eq 4.1): 100 %, 60.6 % and 29.3 %. The relative intensity of the $8^+ \rightarrow 6^+$ transition $I_{\mathrm{rel}}(8^+ \rightarrow 6^+)$ was the parameter. Fig 4.4 shows the sum of the measured $2^+ \rightarrow 0^+$, $4^+ \rightarrow 2^+$ and $6^+ \rightarrow 4^+$ coincidence spectra, which will be referred to as the "total coincidence spectrum" in further text.

To compare the measured and the simulated total coincidence spectra, the intensities of the peaks were normalized to the number of counts in the $2^+ \rightarrow 0^+$, $4^+ \rightarrow 2^+$ and $6^+ \rightarrow 4^+$ peak. The normalized intensities of the $2^+ \rightarrow 0^+$, $4^+ \rightarrow 2^+$ and $6^+ \rightarrow 4^+$ peaks in all simulated total coincidence spectra were in very good agreement with the experimental results. For example, in Table 4.1, the intensities of the measured and simulated ($I_{\mathrm{rel}}(8^+ \rightarrow 6^+)$=5 %) total coincidence spectra are compared to each other. This proves that the simulation with GEANT4 was performed correctly.

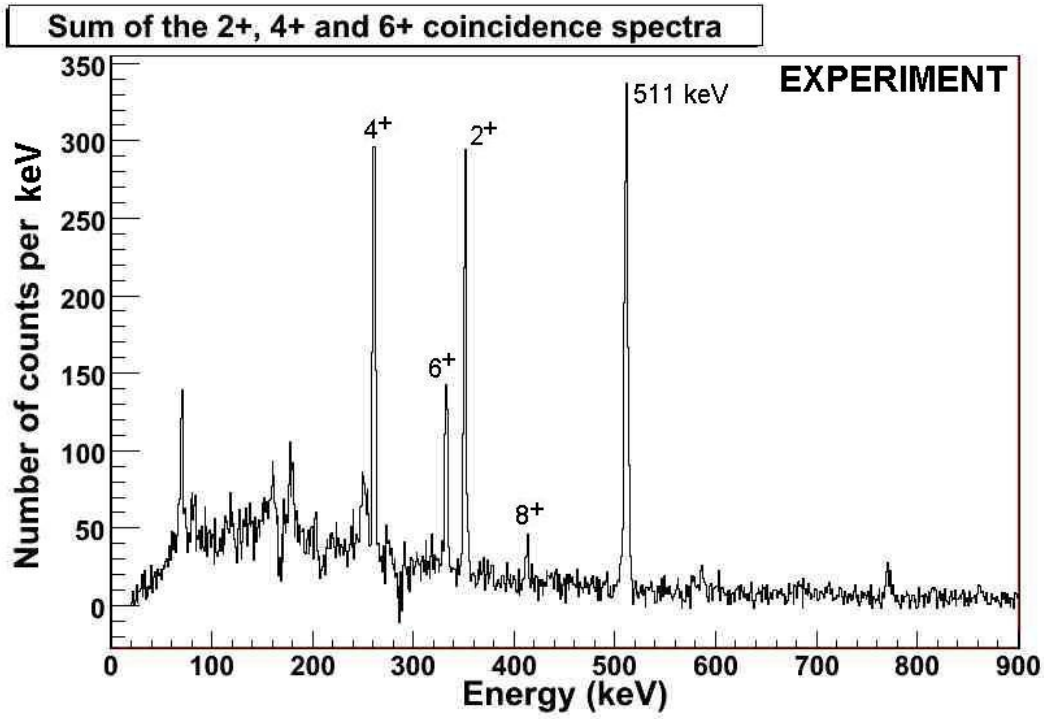

Figure 4.4: Sum of the $2^+ \rightarrow 0^+$, $4^+ \rightarrow 2^+$ and $6^+ \rightarrow 4^+$ coincidence spectra (background subtracted). The number of counts in the peak of the $8^+ \rightarrow 6^+$ transition is 190(20), the sum of the numbers of counts in the $2^+ \rightarrow 0^+$, $4^+ \rightarrow 2^+$ and $6^+ \rightarrow 4^+$ peaks equals 2960(55).

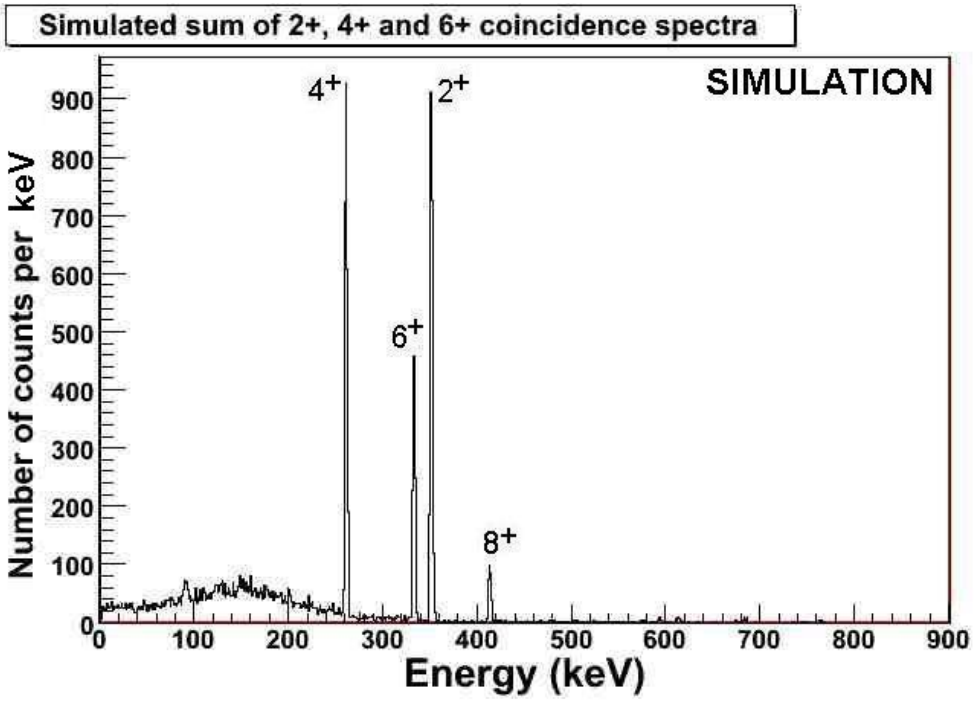

Figure 4.5: Simulated spectrum (by GEANT4) of the sum of the $2^+ \rightarrow 0^+$, $4^+ \rightarrow 2^+$ and $6^+ \rightarrow 4^+$ coincidence spectra, if the $8^+ \rightarrow 6^+$ transition would have a relative intensity equal to 5 %. The number of counts in the peak of the $8^+ \rightarrow 6^+$ transition is 415(20), the sum of the numbers of counts in the $2^+ \rightarrow 0^+$, $4^+ \rightarrow 2^+$ and $6^+ \rightarrow 4^+$ peaks equals 7451(86).

Data was simulated by GEANT4 for $I_{\mathrm{rel}}(8^+ \rightarrow 6^+)$ = 1,2,...,7 %. In Fig 4.6, the intensity of 413 keV in the simulated total coincidence spectrum (normalized to the $2^+ \rightarrow 0^+$, $4^+ \rightarrow 2^+$ and $6^+ \rightarrow 4^+$ number of counts) is plotted as a function of the relative intensity of the $8^+ \rightarrow 6^+$ transition, used as input for the simulation. The intensities in the total coincidence spectra are clearly linearly dependent of the input parameter $I_{\mathrm{rel}}(8^+ \rightarrow 6^+)$.

The measured intensity of the $8^+ \rightarrow 6^+$ peak in the total coincidence spectrum is equal to 0.064(5) (see Table 4.1). According to the simulation, this corresponds to a 5.6(4) % relative intensity of the $8^+ \rightarrow 6^+$ peak in the single spectrum (see Fig 4.6).

In a previous β-decay study of ^{182}Tl [Bou91], a relative intensity of the $8^+ \rightarrow 6^+$ transition of 20 % was reported, see Table 1.1. In the article, it is not mentioned that the 413 keV peak could be a doublet. It is possible that they did not know about the 413 keV transition in the β decay of ^{182}Hg.

	Number of counts in the peak (normalized as explained in the text)			
	$2^+ \to 0^+$	$4^+ \to 2^+$	$6^+ \to 4^+$	$8^+ \to 6^+$
Experiment	0.384(11)	0.404(12)	0.212(8)	0.064(5)
Simulation	0.391(7)	0.402(7)	0.207(5)	0.057(3)

Table 4.1: The number of counts in the different peaks, normalized to the number of counts in the $2^+ \to 0^+$, $4^+ \to 2^+$ and $6^+ \to 4^+$ transition. The simulation was done for $I_{\text{rel}}(8^+ \to 6^+)$=5%.

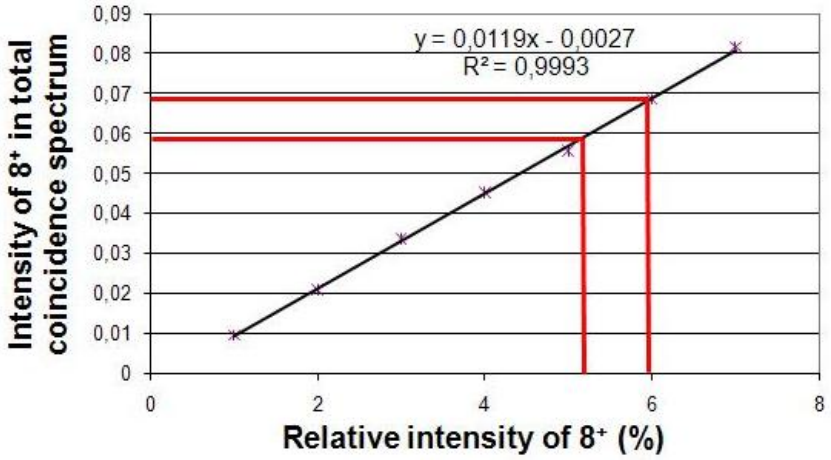

Figure 4.6: The intensity of the $8^+ \to 6^+$ peak in the sum spectrum, normalized to the number of counts in the $2^+ \to 0^+$, $4^+ \to 2^+$ and $6^+ \to 4^+$ peaks, as a function of the relative intensity of the $8^+ \to 6^+$ peak in the single spectrum, simulated by GEANT4.

4.5 Level scheme of ^{182}Hg

Coincidence spectra off all γ peaks coming from ^{182}Tl decay were carefully investigated. The relative intensities, corrected for the efficiency of the detector, are summarized in Table 4.2. For $E2$ transitions, the conversion coefficients were obtained from the *Conversion Coefficient Calculator* [The10]. The $E0$ component of the 196 keV line, is discussed in the next section.

The level scheme of ^{182}Hg, that was obtained by studying all the $\gamma\gamma$-coincidence spectra, is given in Fig 4.7.

E_γ (keV)	Transition	L	$I_{\gamma,rel}$ (%)	$I_{trans,rel}$	Coincident with (♯coincidences):
196.4	$2^+ \rightarrow 2^+$	$E0$	3.5(5)	16(10)[1]	/
261.0	$4^+ \rightarrow 2^+$	$E2$	60.6(9)	66.0(14)	332(♯172), 351(♯605), 413(♯60), 511(♯538), 682(♯40), 769(♯35)
332.6	$6^+ \rightarrow 4^+$	$E2$	29.3(6)	29.6(7)	261(♯175), 351(♯190), 413(♯36) 511(♯167), 547(♯15)
351.3	$2^+ \rightarrow 0^+$	$E2$	100	100.0(15)	261(♯651), 332(♯184), 413(♯21) 511(♯729), 576(♯56), 723(♯27) 747(♯20), 769+772(♯95
413.5	$8^+ \rightarrow 6^+$	$E2$	5.6(4)[2]	5.5(4)	261(♯33), 332(♯37), 351(♯29)
526.5			3.7(6)		/
547.8	$2^+ \rightarrow 0^+$	$E2$	23.2(6)	22.2(7)	511(♯59), 576(♯28), 747(♯32)
576.5			11.4(11)		351(♯23), 511(♯80), 547(♯37)
682.4			9.8(4)		/
723.0			3.3(4)		/
747.8			14.5(6)		511(♯50), 547(♯29), 351(♯12)
769.5			7.4(7)		261(♯25), 351(♯23), 511(♯26)
772.4			11.2(7)		351(♯46), 511(♯22)

Table 4.2: Summary of energies, intensities and coincidences of all γ transitions associated with ^{182}Tl β decay. The intensities were normalized to the strongest transition in ^{182}Hg. $I_{\gamma,\mathrm{rel}}$ is corrected for the efficiency of the detector, while $I_{\mathrm{trans,rel}}$ has also taken the conversion electrons into account. Where there are no coincidences listed, their wasn't enough data to analyze the coincidence spectrum.

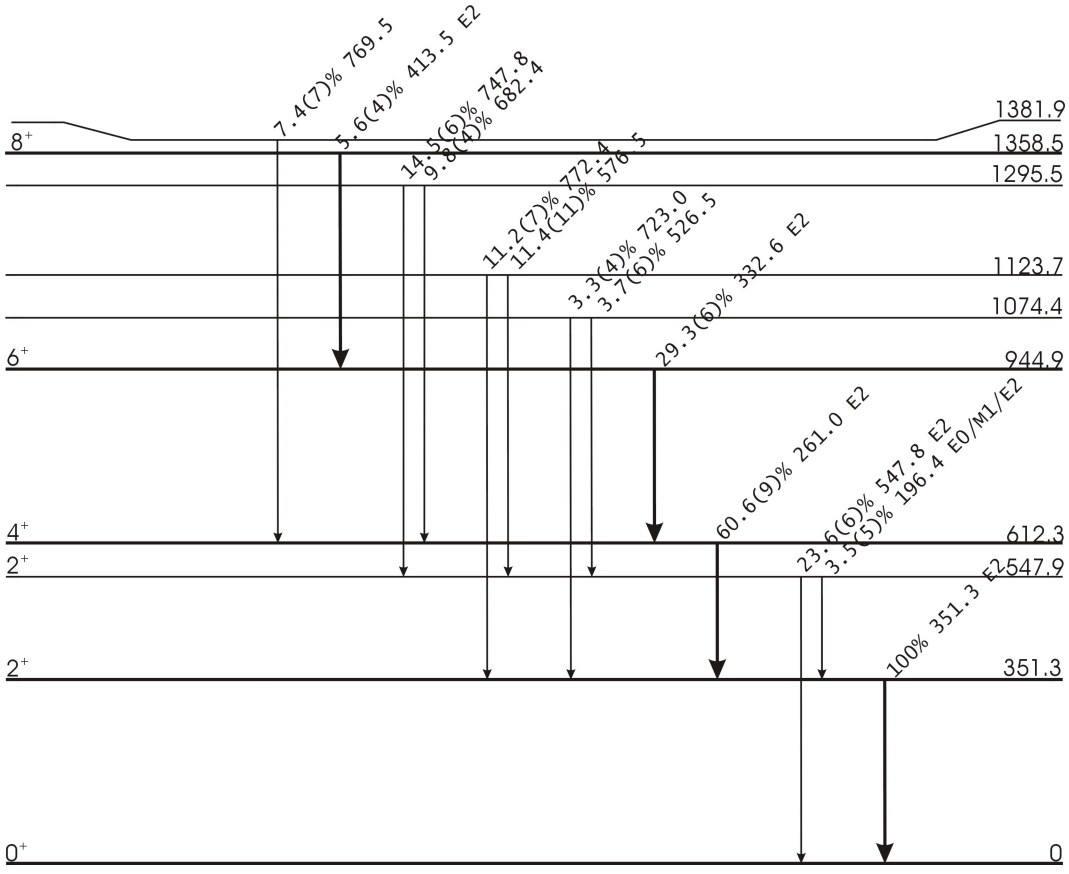

Figure 4.7: Excited level scheme of ^{182}Hg, obtained from ^{182}Tl β decay. The energies and relative intensities of all γ transitions are given.

4.6 $E0$ component in the $2_2^+ \rightarrow 2_1^+$ transition

Fig 4.8(a) gives the spectrum of γ rays in coincidence with the 576 keV line, which is observed in the single spectrum and attributed to the decay of ^{182}Tl, see Fig 4.1. Inspection of the coincidence spectrum shows the 351 keV ($2^+ \rightarrow 0^+$) and 547 keV γ lines. The 547 keV transition is known as a γ line deexciting the second 2^+ state in ^{182}Hg [Bin95, Bre10]. The 196 keV line, observed in the single γ rays spectrum, has the ^{182}Tl half-life behavior and fits to the energy difference between the 2_1^+ and 2_2^+ states. The partial level scheme in Fig 4.8(b) is proposed.

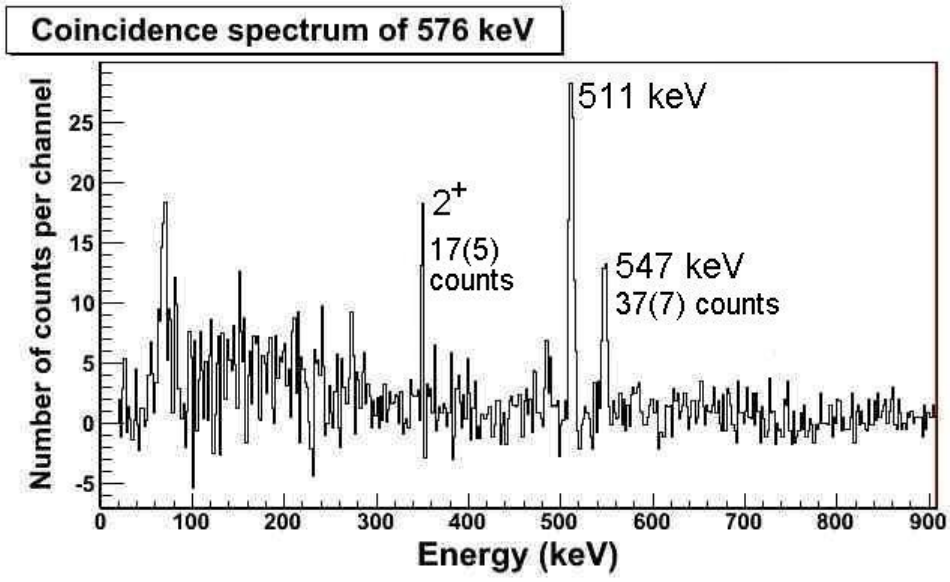

(a)

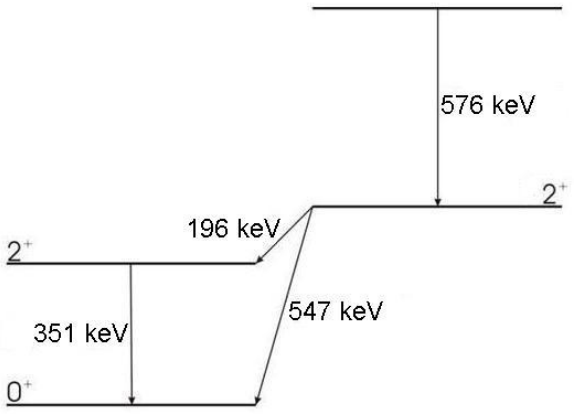

(b)

Figure 4.8: The 576 keV peak is seen in coincidence with 351 keV and 547 keV. The number of counts are corrected for the efficiency of the detector.

From the single γ-rays spectrum, the relative intensities $I_{\text{rel}} = 3.5(5)\,\%$ for the 196 keV γ line and $I_{\text{rel}} = 23.2(6)\,\%$ for the 547 keV γ line were determined, see Table 4.2. The ratio between the two relative intensities is 15 %. According to Fig 4.8(b), both transitions originate from the same level. Corrected for the efficiency, 37(7) γ rays with E_γ=547 keV were observed in coincidence with the 576 keV transition. Since the 547 keV transition and the 196 keV transition are originating from the same state, it can be expected that the ratio of their relative intensities in the single γ-rays spectrum should be the same as in the coincidence spectrum with the 576 keV transition. Therefore 5(1) γ rays should also be observed in coincidence with the 576 keV γ transition. In the coincidence spectrum in Fig 4.8(a), these 5 counts are lost in the background of the spectrum.

The conversion coefficient of the $2^+ \rightarrow 0^+$ transition, with an energy of 351 keV, is equal to 0.0675(10) [The10]. After correction for the ICC, 18(5) transitions with E_γ=351 keV were observed in coincidence with the 576 keV transition. The conversion coefficient of the $2_2^+ \rightarrow 0^+$ transition, with an energy of 547 keV, is equal to 0.0217(3) [The10], therefore 38(7) transitions are in coincidence with the 576 keV transition. The 2_2^+ state deexcites for 18/(18+38)=32(10) % to the 2^+ state and for 38/(18+38)=68(17) % to the ground state. Since the relative transition intensity $I_{trans,rel}$ of the 547 keV line is equal to 22.2(7) %, the relative transition intensity $I_{trans,rel}$ of the 196 keV line is

$$I_{trans,rel}(196\,\text{keV}) = 22.2\,\% \times \frac{32\,\%}{68\,\%} = 10.4(42)\,\% \quad .$$

The internal conversion coefficient ICC is equal to

$$\text{ICC} = \frac{I_{\text{IC}}}{I_\gamma} = \frac{I_{trans,rel} - I_\gamma}{I_\gamma} = \frac{10.4\,\% - 3.5\,\%}{3.5\,\%} = 2.0(7) \ .$$

Since the 196 keV transition has a very short life time (it is in coincidence, <200 ns) and a high ICC in comparison with a $M1$ or $E2$ transition (see Table 4.3), it can be concluded that the transition has an $E0$ component. Multipoles of higher order are excluded by short half life of observed state. Since $E0$ transition is allowed only between states with the same spin and parity, the level with excitation energy 547.9 keV is a 2^+ state.

$E_\gamma = 196\,\text{keV}$	$M1$	$E2$	$M3$	$E4$
ICC	1.17(17)	0.419(6)	25(4)	33.8(5)

Table 4.3: Internal conversion coefficients for a transition with $E_\gamma = 196$ keV and no parity change

4.7 Discussion

4.7.1 Ground state of ^{182}Tl

The lowest orbitals active in the Tl isotopes in this region are $3s_{1/2}$ for the protons and $1i_{13/2}$ for the neutrons. The coupling leads to a 6^+-7^+ multiplet. In β decay typically states with spins differing with ΔI=0,1 will be populated. The relative intensity of the depopulation of the 8^+ state in ^{182}Hg was calculated to be 5.6 %, see Table 4.2. No significant γ lines were found which feed the 8^+ state, see Fig 4.7. Therefore, in present data, the β feeding of the 8^+ state in ^{182}Hg has been unambiguously observed. This suggests a 7^+ assumption for the β decaying state in ^{182}Tl, which is the same configuration as is known in heavier masses.

4.7.2 Systematics of excited states in even-A Hg isotopes

Fig 4.9 gives the known excited states for the even-A isotopes of Hg. In the heavier Hg isotopes, $188 < A < 200$, the ground state band is not changing in function of N. This suggests that they all have the same configuration. The ratio between the energies of the 4^+ and 2^+ states of the ground-state band is about 2.5. Remember that if the nucleus is well deformed, the ratio should be 3.33. It is known that the even-A Hg isotopes have a slightly oblate, almost spherical, ground-state band.

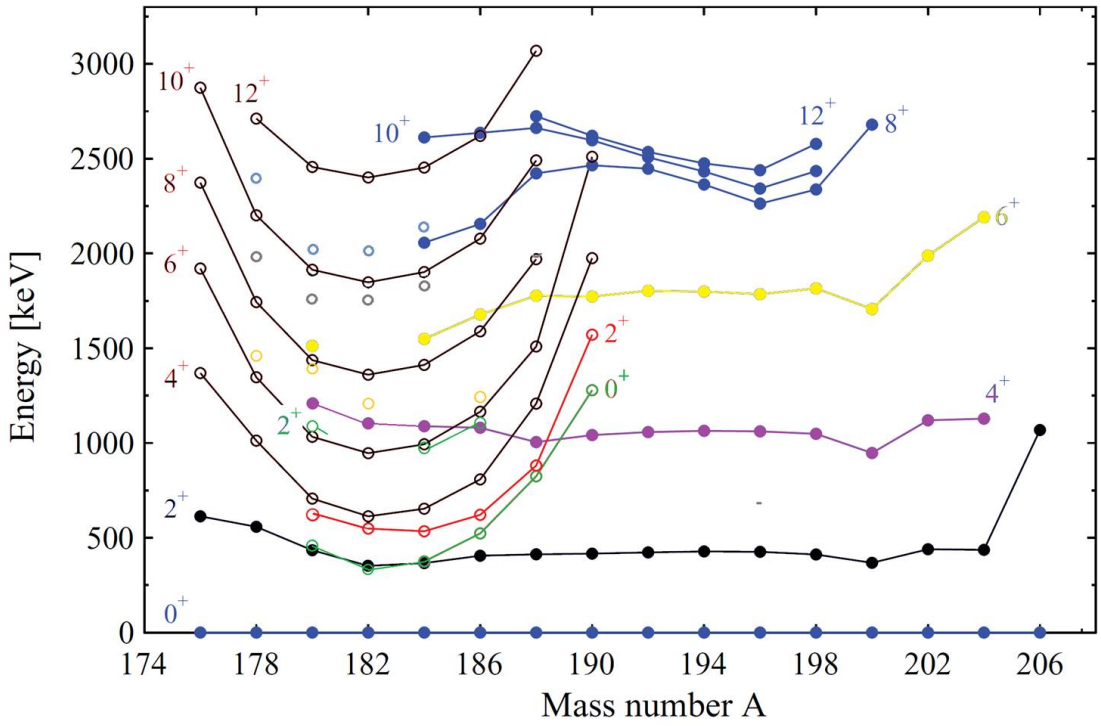

Figure 4.9: Excitation energies for even-A Hg isotopes. The ground state band forms horizontale lines, the deformed band forms parabola.

Approaching the midshell $N = 104$, the nearly spherical ground-state band appeared to be crossed by strongly deformed intruder structure, see Fig 4.9. The excitation energy of the

deformed band head is affected by residual quadrupole-quadrupole proton-neutron interactions between valence protons and neutrons [Woo92]. These interactions are strongest in the vicinity of the neutron midshell. Therefore excitation energies of the deformed rotational bands in function of the mass number A follow a parabolic trend, with a minimum at $N = 104$

4.7.3 Two level mixing

When approaching the neutron midshell in Fig 4.9, levels with the same spin and parity come close together and the levels mix as explained in Section 1.1.4. Due to this mixing, the ground state band is also affected slightly. For Hg isotopes with $A < 188$, Fig 4.9 shows that the first 4^+ state is actually coming from the deformed band. The 4^+ state observed in this thesis, is an excited state from the deformed rotational band. The same applies to the observed 6^+ and 8^+ states. The second 4^+ state, coming from the ground state band, has two possible candidates in the level scheme in Fig 4.7: 1123 keV and 1074 keV, since both of them decay to the first and second 2^+ state. More data could be able to derive which one is the second 4^+ state, originating from the ground state band.

The observed $E0$ component in the transition between the first and second 2^+ states, proves not only that the two levels are mixed, but moreover that they have a different deformation. This demonstrates that in ^{182}Hg coexisting structures are present at low excitation energy.

Chapter 5

Conclusion

The first part of the thesis concentrated on the α decay study of ^{200}Fr. The second part of the thesis involved the study of γ rays subsequent to the β decay of ^{182}Tl. Both experiments were performed at the ISOLDE facility at CERN. The windmill chamber was used, in combination with 4 Si detectors and a Miniball cluster with three Ge crystals.

The two experiments were related to the study of β-delayed fission. βDF decay was recently discovered in ^{196}At. The α decay study of ^{200}Fr was dedicated to deduce improved value for the β-branching ratio of its daughter nucleus ^{196}At. Taking the recoil effect of the daughter nucleus into account, the value of $b_{\mathrm{EC}/\beta^+}(^{196}\mathrm{At})$ was determined to be 9(6) %. Averaging with the previously obtained value [Wit05], the new value for $b_{\mathrm{EC}/\beta^+}(^{196}\mathrm{At})$ was established to be 7(4) %.

βDF was also observed recently in ^{182}Tl. The γ rays coming from the EC/β^+ decay were studied in order to gain information on the nuclear structure of ^{182}Tl and ^{182}Hg. The half life of ^{182}Tl $T_{1/2} = 2.9(4)$ s was deduced. Averaging with the previously obtained value [Ach09], the half life of ^{182}Tl was established to be $T_{1/2} = 2.9(3)$ s.

The coincidence spectra of γ lines coming from ^{182}Tl β decay, were investigated. In this way, the level scheme of ^{182}Hg was constructed. Since the 413 keV γ line was a doublet, the relative intensity of the $8^+ \rightarrow 6^+$ transition had to be determined by comparing the experimental results and the simulated data by GEANT4 package.

An $E0$ component in the transition was observed between two 2^+ states, a fingerprint for mixing of the states having different deformations. This proves the appearance of the phenomenon of shape coexistence in ^{182}Hg.

Finally, since there is β feeding of the 6^+ and 8^+ state in ^{182}Hg, it can be concluded that most probably the β decaying state of ^{182}Tl is a 7^+ state, with a $\pi(3\mathrm{s}_{1/2})^{-1}$, $\nu(1\mathrm{i}_{13/2})$ configuration. The same structure is known in heavier even-A Tl isotopes.

Bibliography

[Ach09] E. Achterberg et al. Nuclear data sheets for $a = 178$. *Nuclear Data sheets*, 110 (2009) 1677.

[And] A.N. Andreyev et al. In preparation.

[Bin95] K.S. Bindra et al. Prolate-oblate band mixing and new bands in ^{182}hg. *Phys. Rev. C*, 51(1) (1995) 401–404.

[Bou91] A. Bouldjedri et al. Identification and decay of ^{182}tl. *Z. Phys. A*, 339 (1991) 311–312.

[Bre10] N. Bree. *In preparation.* PhD thesis, University of Leuven, Faculteit Wetenschappen, 2010.

[Cai74] M. Cailliau. Un noyau loin de la stabilité: Le $^{182}_{78}$pt. *Journ. de Phys.*, 35 (1974) 233–236.

[Can10] Canberra. `http://www.canberra.com`, 2010.

[Cas90] R.F. Casten. *Nuclear Structure from a Simple Perspective.* Oxford University Press, 1990.

[Coc10] T.E. Cocolios. *Single-Particle and Collective Properties around Closed Shells probed by In-Source Laser Spectroscopy.* PhD thesis, University of Leuven, Faculteit Wetenschappen, 2010.

[Ebe01] J. Eberth et al. Miniball, a ge detector array for radioactive ion beam facilities. *Progr. Part. Nucl. Phys.*, 46 (2001) 389–398.

[Els09] J. Elseviers. *Electron Capture Delayed Fission of ^{180}Tl.* Master's thesis, University of Leuven, Faculteit Wetenschappen, 2009.

[Fed03] V.N. Fedoseyev et al. Atomic spectroscopy studies of short-lived isotopes and nuclear isomer separation with the isolde rilis. *Nucl. Instr. Meth. B*, 204 (2003) 353.

[Fir99] R.B. Firestone, V.S. Shirley, C.M. Baglin, S.Y.F. Chu, and J. Zipkin. *Table of Isotopes.* John Wiley & Sons, 1999.

[ISO10] ISOLDE website. `http://isolde.web.cern.ch/ISOLDE/`, 2010.

[Kan84] J. Kantele. Heavy ions and nuclear structure. *Harwood Academic*, 1984391. Proceedings of the XIV Summer School, Mikolajki.

[Kno99] G.F. Knoll. *Radiation Detection and Measurement*. John Wiley, 1999.

[Kra88] K.S. Krane. *Introductory Nuclear Physics*. John Wiley, 1988.

[Laz87] Yu.A. Lazarev et al. Observation of delayed nuclear fission in the region of ^{180}hg. *Europhys. Lett.*, 4(8) (1987) 893–898.

[May49] M.G. Mayer. On closed shells in nuclei. *Phys. Rev.*, 75 (1949) 1969–1970.

[MIN10] MINIBALL website. `http://www.miniball.york.ac.uk/`, 2010.

[Moo70] C.E. Moore. Ionization potentials and ionization limits derived from the analysis of optical spectra. *Nat. Stand. Ref. Data Syst.*, 34 (1970) .

[Nat10] National Nuclear Data Center. `http://www.nndc.bnl.gov/`, 2010.

[Ort10] Ortec. `http://www.ortec-online.com`, 2010.

[Pet08] A. Petts et al. Lifetime measurements and coulomb excitation of light hg nuclei. *American Institute for Physics*, 2008414–418.

[SRI08] SRIM-The Stopping and Range of Ions in Matter. `http://www.srim.org/`, 2008.

[The10] The Australian National University. `http://physics.anu.edu.au/nuclear/bricc/`, 2010.

[Ven10] M. Venhart, 2010. private communication.

[Wit05] H. De Witte et al. Alpha-decay of neutron-deficient ^{200}fr and heavier neighbors. *Europhys. Journ. A*, 23 (2005) 243–247.

[Woo92] J.L. Wood et al. *Coexistence in Even-Mass Nuclei*. Physics Reports, 1992.